

AEDC-TR-09-T-5



## Pulsed Electron Beam Spectroscopy for Temperature Measurements in Hypersonic Flows

**Final Report Submitted to  
High-Speed/Hypersonic Test Focus Area  
of the Test and Evaluation/Science  
and Technology Program**

**Andy Nelius and Joe Wehrmeyer  
Aerospace Testing Alliance**

**January 2010**

**Final Report for Period 16 November 2004 – 31 January 2009**

**Statement A:** Approved for public release; distribution is unlimited.

**ARNOLD ENGINEERING DEVELOPMENT CENTER  
ARNOLD AIR FORCE BASE, TENNESSEE  
AIR FORCE MATERIEL COMMAND  
UNITED STATES AIR FORCE**

## NOTICES

When U. S. Government drawings, specifications, or other data are used for any purpose other than a definitely related Government procurement operation, the Government thereby incurs no responsibility nor any obligation whatsoever, and the fact that the Government may have formulated, furnished, or in any way supplied the said drawings, specifications, or other data, is not to be regarded by implication or otherwise, as in any manner licensing the holder or any other person or corporation, or conveying any rights or permission to manufacture, use, or sell any patented invention that may in any way be related thereto.

Qualified users may obtain copies of this report from the Defense Technical Information Center.

References to named commercial products in this report are not to be considered in any sense as an endorsement of the product by the United States Air Force or the Government.

## DESTRUCTION NOTICE

For unclassified, limited documents, destroy by any method that will prevent disclosure or reconstruction of the document.

## APPROVAL STATEMENT

### Prepared by:



ANDY NELIUS  
Aerospace Testing Alliance



JOE WEHRMEYER  
Aerospace Testing Alliance

### Reviewed by:



STEVEN BANCROFT  
Air Force Project Manager  
649 TESS Test Systems Squadron

### Approved by:



THOMAS P. FETTERHOFF  
Technical Director  
649th Test Systems Squadron

<b>REPORT DOCUMENTATION PAGE</b>				<i>Form Approved OMB No. 0704-0188</i>
<p>The public reporting burden for this collection of information is estimated to average 1 hour per response, including the time for reviewing instructions, searching existing data sources, gathering and maintaining the data needed, and completing and reviewing the collection of information. Send comments regarding this burden estimate or any other aspect of this collection of information, including suggestions for reducing the burden, to Department of Defense, Washington Headquarters Services, Directorate for Information Operations and Reports (0704-0188), 1215 Jefferson Davis Highway, Suite 1204, Arlington, VA 22202-4302. Respondents should be aware that notwithstanding any other provision of law, no person shall be subject to any penalty for failing to comply with a collection of information if it does not display a currently valid OMB control number.</p> <p><b>PLEASE DO NOT RETURN YOUR FORM TO THE ABOVE ADDRESS</b></p>				
1. REPORT DATE (DD-MM-YYYY)  xx-01-2010		2. REPORT TYPE  Final Report	3. DATES COVERED (From – To)  16 Nov 2004 – 31 Jan 2009	
4. TITLE AND SUBTITLE  Pulsed Electron Beam Spectroscopy for Temperature Measurements in Hypersonic Flows		5a. CONTRACT NUMBER		
		5b. GRANT NUMBER		
		5c. PROGRAM ELEMENT NUMBER		
6. AUTHOR(S)  Nelius, Andy and Wehrmeyer, Joe Aerospace Testing Alliance		5d. PROJECT NUMBER  11172		
		5e. TASK NUMBER		
		5f. WORK UNIT NUMBER		
7. PERFORMING ORGANIZATION NAME(S) AND ADDRESS(ES)  Arnold Engineering Development Center			8. PERFORMING ORGANIZATION REPORT NO.  AEDC-TR-09-T-5	
9. SPONSORING/MONITORING AGENCY NAME(S) AND ADDRESS(ES)  DoD Test Resources Management Center, TE/ST-Hypersonics Focus Area			10. SPONSOR/MONITOR'S ACRONYM(S)	
			11. SPONSOR/MONITOR'S REPORT NUMBER(S)	
12. DISTRIBUTION/AVAILABILITY STATEMENT  <b>Statement A:</b> Approved for public release; distribution is unlimited.				
13. SUPPLEMENTARY NOTES  Available in the Defense Technical Information Center (DTIC).				
14. ABSTRACT  Reports development of pulsed electron beam system for nonintrusive temperature measurements of hypersonic flows.				
15. Subject Terms  Gas phase optical spectroscopy, hypersonic wind tunnel testing, nitrogen spectroscopy.				
16. SECURITY CLASSIFICATION OF:  A. REPORT Unclassified		17. LIMITATION OF ABSTRACT  Same as Report	18. NUMBER OF PAGES  43	19A. NAME OF RESPONSIBLE PERSON  Joseph A. Wehrmeyer
B. ABSTRACT Un classified				19B. TELEPHONE NUMBER (Include area code)  931-454-4345

Standard Form 298 (Rev. 8/98)  
Prescribed by ANSI Std. Z39-18

## PREFACE

The work reported herein was conducted by the Arnold Engineering Development Center (AEDC), Air Force Materiel Command (AFMC), at the request of the DoD Test Resources Management Center, TE/ST Hypersonics Focus Area. The results of the project were obtained by the Aerospace Testing Alliance (ATA), the operations, maintenance, information management, and support contractor for AEDC, AFMC, Arnold AFB, TN. Testing for the project was conducted in the Laboratory Shock Tunnel of the Building 934 Laser Lab from November 2004 to December 2008 under Air Force Project Number 11172. The Sponsor Test and Evaluation Manager was Tom Fetterhoff, the Air Force Project Manager was Captain Rod Koch, and the ATA Project Manager was John Prebola.

## CONTENTS

	<u>Page</u>
Acknowledgment.....	3
Abstract .....	3
1.0 Introduction .....	4
2.0 Pulsed E-Beam System for Measurement at Relatively High Pressure and Density.....	5
3.0 Pulsed E-Beam Fluorescence Considerations.....	7
4.0 Application of Pulsed E-Beam Gun to High-Pressure Flows.....	9
5.0 Density Measurement with the Pulsed E-Beam Technique .....	14
6.0 Pulsed E-Beam N <sub>2</sub> <sup>+</sup> Emission Spectra for Temperature Measurement .....	15
7.0 Application of Pulsed E-Beam System to Hypersonic Flow .....	17
8.0 Summary .....	20
References .....	22

## FIGURES

### Figure

1. Schematic of "Traditional" Continuous E-Beam System Mounted on Flow Facility. ....	4
2. Schematic of Differential Pressure Pump Used at AEDC to Provide Pressure Separation up to 3 torr. From Ref. 6.....	5
3. Energy Level Diagram for N <sub>2</sub> and N <sub>2</sub> + .....	6
4. Schematic of Pulsed E-Beam Gun.....	7
5. Schematic of Signal Strength to Concentration Relationship for Continuous E-Beam Excitation. ....	8
6. Schematic of Temporal Features of Pulsed E-Beam System. ....	8
7. Relationship Between (0-0) N <sub>2</sub> + Emission Band Strength and N <sub>2</sub> Density for Three Different Detector Integration Times. ....	9
8. Photograph of 27-kV Pulsed E-Beam Gun in Operation Using N <sub>2</sub> at 70 mtorr.....	9
9. Schematic of Differential Pressure Pump Configurations: a) Both Orifices Used, b) Long Orifice Used at Bottom, c) Long Orifice Used at Top, and d) Short Orifice Used at Top. ....	10
10. Photograph of Pulsed E-Beam System Located at AEDC Laboratory Shock Tunnel....	11
11. Performance of Differential Pressure Pump Using 140-cfm Roots Blower Vacuum Pump.....	11
12. Conceptual Drawing of FARVA Showing Rotating Disk at Bottom. ....	12
13. Schematic of Equipment Used for Timing of FARVA and Pulsed E-Beam Gun. ....	12

14.	Photograph Showing Placement of FARVA and Pulsed E-Beam Gun on Dump Tank of 12AEDC Shock Tunnel. ....	12
15.	Wiring Schematic for FARVA Programmable Motor Controller. ....	13
16.	Time History of FARVA Valve with 28-Deg "Windup." ....	13
17.	Experimental Relationship Between (0-0) N <sub>2</sub> <sup>+</sup> Emission Band Strength and N <sub>2</sub> Density for 30-nsec Detector Integration Times. ....	14
18.	Calculated N <sub>2</sub> <sup>+</sup> (0-0) Emission Spectra at 300 and 2,000 K (Instrumental Width: 0.05 nm). ....	15
19.	Experimental N <sub>2</sub> <sup>+</sup> Emission Spectrum Compared to Theoretical Spectrum at 297 K. ....	16
20.	Calculated N <sub>2</sub> <sup>+</sup> Emission Spectra at Four Combinations of Vibrational (T <sub>v</sub> ) and Rotational (T <sub>r</sub> ) Temperatures. ....	16
21.	Ratio of (1,1) to (0,0) N <sub>2</sub> <sup>+</sup> B-X Emission vs. Vibrational Temperature. ....	17
22.	Schematic of AEDC Laboratory Shock Tunnel. ....	17
23.	N <sub>2</sub> <sup>+</sup> and N <sub>2</sub> Neutral Spectra Obtained at Two Different Times After Bursting of Shock Tunnel Diaphragm. N <sub>2</sub> Flow Conditions at Nozzle Exit: Mach Number = 7.5 and Exit Static Temperature = Approximately 700 °F Based on Ideal Shock Theory. Dump Tank Pressure 650 mtorr. ....	18
24.	Time History of Shock Tunnel Pressures at K1 and K6, Along with Signal from FARVA to Trigger ICCD and Pulsed E-Beam Gun. ....	19
25.	Pulsed E-Beam Spectra from AEDC Laboratory Shock Tunnel Using Spectrograph with 0.5-nm Resolution. Best-Fit Theoretical Spectrum is for 170 K. ....	20

## APPENDICES

### Appendix

A.	Software Code for FARVA Motor Controller .....	25
B.	Literature Survey of Molecular Collisional Quenching Data.....	26
C.	Improvements to Pulsed E-Beam System .....	30

## ACKNOWLEDGMENT

The authors would like to thank the Test Resource Management Center (TRMC) Test and Evaluation/Science and Technology (T&E/S&T) Program for their support. This work is funded by the T&E/S&T Program through the Arnold Engineering Development Center, Arnold Air Force Base, TN.

## ABSTRACT

A pulsed electron-beam system has been developed at the Arnold Engineering Development Center (AEDC) for use in relatively high-pressure hypersonic shock and wind tunnels used for airbreathing propulsion system development. The high-current, short-duration pulse of electrons produced by a pulsed e-beam gun allows the resulting  $N_2^+$  fluorescence to be detected during a short (~100 nsec) time period. This enables nonintrusive static temperature measurements in blowdown hypersonic flow tunnels, such as in AEDC's Tunnel 9 or Aerodynamic Propulsion Test Unit facilities or short duration facilities such as HyPulse.

The operational pressure of a pulsed e-beam gun (~70 mtorr) is higher than for a continuous e-beam gun (~0.1 mtorr), which enables the investigation of hypersonic flows, using pulsed e-beam fluorescence, to pressure altitudes as low as 60,000 ft. This is a much lower pressure altitude than can be examined by continuous e-beams and opens the opportunity to use pulsed e-beam systems in the development of airbreathing hypersonic propulsion. However, the pulsed e-beam gun still requires a single-stage pressure barrier between it and the relatively high-pressure scramjet flowfield (~1 to 76 torr). Pressure separation up to ~1 torr is provided by a differential pressure pump unit. For pressures from 1 to 50 torr, a second pressure separation device, a fast action rotary valve assembly, has been built. The valve initially had a 12 millisecond delay between the time it receives a trigger signal and the time it completely opens, allowing the pulsed e-beam to fire into the test medium although further refinements of the valve allow it to operate with a 3.5 millisecond delay. The valve stays open for 150 microseconds, which is enough time to allow the pulsed e-beam to travel through the hole and yet is also a short-enough time to guard against a build up to a significant pressure that prevents pulsed e-beam operation. The spectral shape of the  $N_2^+$  fluorescence caused by the pulsed e-beam is used to simultaneously measure both rotational and vibrational temperature. The relative strength of the (0-0) vibrational band fluorescence, at 391 nm, is compared to the (1-1) band at 386 nm in order to deduce vibrational temperature. Rotational temperature is determined by comparing the shape of the (0-0) band to several simulated spectra, each for a different rotational temperature. The temperature associated with the best-fitting simulation provides the measured rotational temperature value.

The pulsed e-beam system has been used on the AEDC Laboratory Shock Tunnel at pressures in its test section of either 1 or 10 torr. The tunnel produces a short-duration, Mach 7.5 nitrogen or air flow using a nonoptimized conical nozzle. For one run at a test cabin pressure of 1 torr and a driver pressure of 550 psig, matching the experimental  $N_2^+$  spectrum to simulated spectra shows significant vibrational nonequilibrium in the flow as well as significant contamination of the test medium with the helium driver gas. Another test at 10 torr driven gas pressure and 850 psig driver gas pressure showed a surprisingly low rotational temperature for the test medium exiting the nozzle. These shock tunnel measurements demonstrate the pulsed e-beam system's capability for rotational and vibrational temperature measurement, but this present work has not found that the pulsed e-beam technique can be used for  $N_2$  density measurement at densities of the order of  $10^{15}$  molecules/cm<sup>3</sup> or greater. Unfortunately, no systematic relationship was found between normalized  $N_2^+$  fluorescence signal and  $N_2$  density for this density range.

## 1.0 INTRODUCTION

A continuous beam of energetic electrons, with energy in the ten s of kilovolt range, can travel tens of centimeters through air if it is at sufficiently low density. In their flight through air the electrons collide with the ambient gas, resulting in several types of molecular processes including ionization, electronic excitation, and subsequent fluorescence of the pre-existing neutral gases and the newly produced ionic species. Detection of this fluorescence can provide information about the densities of the gas species present and can even provide rotational and vibrational gas temperature measurements.<sup>1,2</sup>

The e-beam technique has been applied to hypersonic flow measurements at the Arnold Engineering Development Center<sup>3,4,16</sup> and at the Boeing Hypersonic Shock Tunnel,<sup>5</sup> as well as at other facilities. These applications have used an e-beam system that employs an e-beam gun producing millamp levels of continuous current. Low pressures of the order of 0.1 mtorr are required for the gun to operate. A schematic of an e-beam system using a continuous e-beam gun is shown in Fig. 1. This figure shows that the electrons coming from a heated filament in the gun are accelerated to near-relativistic velocities by passing through one or more high-voltage anodes before passing through a final grounded anode. Magnets along the e-beam path shape and steer the beam before it enters the hypersonic test medium. Figure 1 also shows that the light created by the interaction of the e-beam and the test medium is detected with a photomultiplier tube (PMT) whose output signal is an electrical current proportional to the amount of light sensed by the photomultiplier tube. Selective detection of light emitted by only one gas species is accomplished by placing optical filters in front of the PMT to only allow light for that species to strike the PMT. Another instrument shown in Fig. 1 is a Faraday cup that collects and measures the e-beam current  $i_{e\text{-beam}}$ . The PMT's output current,  $i_{pmt}$ , is proportional to the density of the particular gas species,  $\rho_j$ , whose light signal passes through the filters. The  $i_{pmt}$  signal is also proportional to  $i_{e\text{-beam}}$ , so the following equation can be obtained:

$$\rho_j = \frac{i_{pmt}}{i_{e\text{-beam}}} C_j f(T, \rho_1, \rho_2, \dots, \rho_K) \quad (1)$$

where  $C_j$  is a calibration coefficient that takes into account detector efficiency and other experimental parameters that remain constant for the experimental setup. The above equation also contains a function  $f$  that accounts for "collisional quenching" of the e-beam fluorescence. Quenching becomes more pronounced at higher densities and temperatures and tends to reduce and eventually eliminate  $i_{pmt}$  no matter what the strength of the e-beam current. Appendix II of this final report contains a literature review of quenching rates for various gases. This review was put together as a subcontract of this work.

Each gas species  $j$  of the total  $K$  that make up the test medium gas mix has its own unique contribution to the quenching function  $f$ , and at low densities and temperatures the value of  $f$  can be normalized to one by using a proper choice of the constant  $C_j$ . At higher densities and

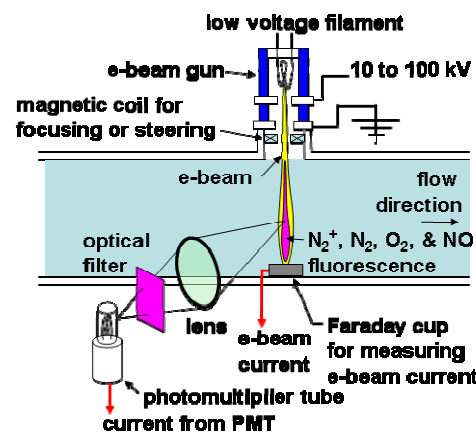


**Figure 1. Schematic of "Traditional" Continuous E-Beam System Mounted on Flow Facility.**

pressures the value of  $f$  will rise above one to account for collision quenching. Usually densities of  $10^{16}$  molecules/cm<sup>3</sup> or less are sufficiently low to allow  $f$  to be unity and hence obviate the need to simultaneously measure all gas species to calculate  $f$ . At 300 K a density of  $10^{16}$  molecules/cm<sup>3</sup> corresponds to a pressure of 0.001 atm or a pressure altitude of 160,000 ft. Thus e-beam techniques have historically examined low density flows usually associated with the simulation of hypersonic flight vehicles undergoing atmospheric re-entry.

Besides signal nonlinearity issues, another problem with the application of the continuous e-beam technique to high-density flows is that the gun must operate around 0.1 mtorr. To fire the gun into flows above this pressure requires a "pressure barrier" that separates the low-pressure gun from the higher pressure test medium it is probing. Some continuous e-beam work at AEDC<sup>6</sup> has been at pressures up to  $10^{17}$  molecules/cm<sup>3</sup> (3 torr at 300 K), and this work required a two-stage "differential pump" that is essentially two thick orifices in series that drop the pressure of gas leaking into the gun, while still allowing the thin e-beam to pass through them. Figure 2 shows a schematic of the two-stage differential pump used at AEDC. Its performance, of course, is limited by the volumetric flowrate of the vacuum pumps connected to it.

Temperature measurements are obtained by replacing the PMT and optical filter shown in Fig. 1 with a spectrograph and linear array detector. Thus the collected fluorescence is dispersed according to its wavelength across the linear array so that the influence of temperature upon the shape of the molecular spectrum can be determined.

## 2.0 PULSED E-BEAM SYSTEM FOR MEASUREMENT IN RELATIVELY HIGH PRESSURE AND DENSITY

The test and evaluation needs of hypersonic flight vehicles that use airbreathing propulsion require an e-beam technique that can be used at the operational altitudes of scramjet engines. For example, a 60,000-ft density altitude corresponds to approximately  $2.5 \times 10^{18}$  molecules/cm<sup>3</sup>, which is about 25 times greater than the maximum density examined by e-beams at AEDC.<sup>6</sup> This is the motivation for the search for a replacement technique for the traditional continuous e-beam technique.

Laser spectroscopy is an attractive alternative to e-beam spectroscopy for many applications, but several hypersonic test facilities, such as AEDC's Tunnel 9, use only N<sub>2</sub> as the test medium. E-beam spectroscopy has continued to prove useful over the years because of its ability to excite N<sub>2</sub>, which is difficult to probe using laser-based fluorescence techniques, especially when the static temperature is near the condensation temperature of N<sub>2</sub>. The reason for the difficulty in using lasers for N<sub>2</sub> fluorescence is shown in Fig. 3, which is an energy level diagram for N<sub>2</sub>.

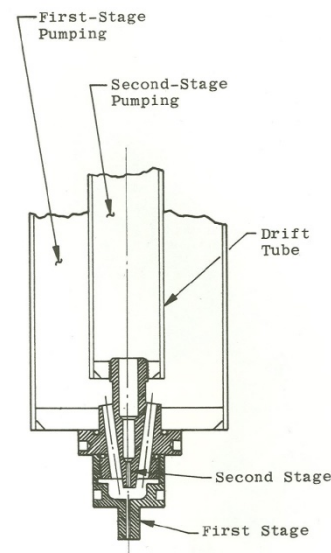


**Figure 2. Schematic of Differential Pressure Pump used at AEDC to Provide Pressure Separation up to 3 torr. From Ref. 6.**

The energy difference between the X and A states of  $N_2$  is approximately 6.2 eV; thus a deep UV-tunable laser source around 200 nm is required for laser-induced fluorescence. Instead of light excitation, an e-beam causes fluorescence via primary electrons striking ground state  $N_2$ , transferring enough energy to ionize  $N_2$  and even causing the resulting  $N_2^+$  ion to be electronically excited. The B state of  $N_2^+$  results in significant fluorescence, with the four strongest emission bands being shown in Fig. 3. Of these four, the (0,0) band at 391 nm is the strongest and is the one most used for density and temperature measurements although the (0,1) and (0,2) bands provide the violet color visible along the e-beam path. It is generally assumed that the rotational and vibrational distributions of the nascent  $N_2^+$  population mimic those of ambient  $N_2$ . This assumption is made because the short duration of the electron-molecule collision does not provide enough time for energy to be added to the rotational or vibrational energy storage modes.<sup>2</sup> Additionally, it is often assumed that the  $N_2^+$  population and its resulting fluorescence are directly proportional to the  $N_2$  population, but this assumption becomes increasingly invalid as density increases above  $10^{16} \text{ cm}^{-3}$ .

In an effort to apply the e-beam fluorescence technique to higher density flows, Prof. E. P. Muntz and co-workers at the University of Southern California used a novel device called a "pulsed electron beam gun" to experimentally investigate  $N_2^+$  and xenon<sup>8</sup> in a static cell using pulsed e-beam spectroscopy. Because of their equipment limitations, they experimentally showed a linear signal variation between fluorescence and gas density up to only  $10^{15} \text{ molecules/cm}^3$ . However, as shown in Section III of this report, the pulsed e-beam technique theoretically should provide signals that are linear with density up to  $10^{18} \text{ molecules/cm}^3$  (corresponding approximately to air at 0.1 atm and 300 K). This density is two orders of magnitude higher than the densities that the continuous e-beam technique can linearly investigate.

The pulsed e-beam gun is based on a pseudo-spark discharge design, which involves the gun operating on the low-pressure side of the Paschen curve minimum.<sup>9</sup> A schematic of the pulsed e-beam gun at AEDC,<sup>10</sup> which is similar to that at the University of Southern California (USC),<sup>11</sup> is shown in Fig. 4. The gun discharges when a spark is created between a trigger electrode and the gun's main cathode, which is connected to a large capacitor charged to tens of thousands of volts. The electrons released in the triggering spark allow a large current to begin flowing from the gun's main cathode to the anode, and in so doing the current escapes the gun through a hole in the anode. In order to work, this gun must have the correct pressure (~70 mtorr) and the correct gas (argon or nitrogen).

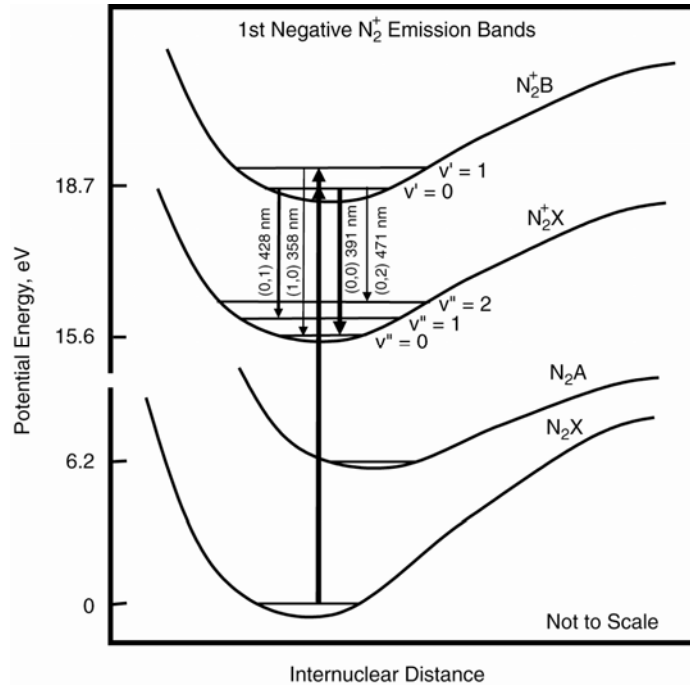


**Figure 3. Energy Level Diagram for  $N_2$  and  $N_2^+$ .**

While continuous e-beams have currents on the order of millamps, pulsed e-beam guns can produce peak currents well over 100 amps in magnitude, with pulse lengths of approximately 60 nsec. For wind and shock tunnel diagnostics, pulsed e-beams have three major advantages over continuous e-beams. The first advantage is that by using a gated, intensified CCD camera that is synchronized with the e-beam pulse, investigators can detect the fluorescence signal while suppressing the detection of continuous emission coming from hot surfaces, particles, or continuous gaseous emission. The second advantage, which is in the same vein as the first, is that the strong pumping by the pulsed e-beam results in a stronger fluorescence signal, compared to background signal, during the pulsed fluorescence time period. For example, 200 amps over 60 nsec should produce the equivalent amount of signal as a 10 milliamp system operating for 1.2 msec. Thus the first two advantages result in improved signal/noise ratio over continuous e-beam systems and a shorter exposure time.

The third advantage of a pulsed e-beam is that a linear relationship between fluorescence signal and number density is maintained for much higher densities than those for continuous e-beams.<sup>7</sup> This allows quantitative density measurements to be made for number densities up to  $\sim 10^{18} \text{ cm}^{-3}$ . The higher number density corresponds to standard atmospheric altitudes of  $\sim 60,000 \text{ ft}$ . Thus a pulsed e-beam gun opens up the use of quantitative e-beam spectroscopy to several wind tunnels at AEDC and elsewhere that are closed to continuous e-beam work because of their relatively high operational pressures.

### 3.0 PULSED E-BEAM FLUORESCENCE CONSIDERATIONS

To clarify the theoretical ability of a pulsed e-beam to extend signal linearity into higher density flows, the following background is presented. Fluorescence occurs as a molecule drops from an electronically excited state down to a lower electronic state, giving up the difference in energy between the two states in the form of light. The fluorescence signal,  $I$ , is proportional to the number density,  $n$ , of the fluorescing species and is also related to other parameters such as the strength of the e-beam current, etc. If all of the other parameters can be considered constant, then  $I$  is equal to the product of  $n$  times a calibration constant  $C_1$ :

$$I = C_1 n \quad (2)$$

However, a second channel exists whereby molecules exit from the excited state without giving off any fluorescence signal. This "quenching" channel involves molecular collisions that transfer the electronic energy into translational energy or other modes without the emission of light. The quenching channel's relative strength compared to that of the fluorescence channel is related to  $n$ , and Eq. (2) can be modified to account for the loss of fluorescence signal attributable to quenching by dividing  $C_1$  by the term  $(1 + C_2 n)$ , where  $C_2$ , another constant, accounts for the relative importance of the collision rate compared to the spontaneous emission rate.<sup>2</sup> Hence Eq. (2) becomes:

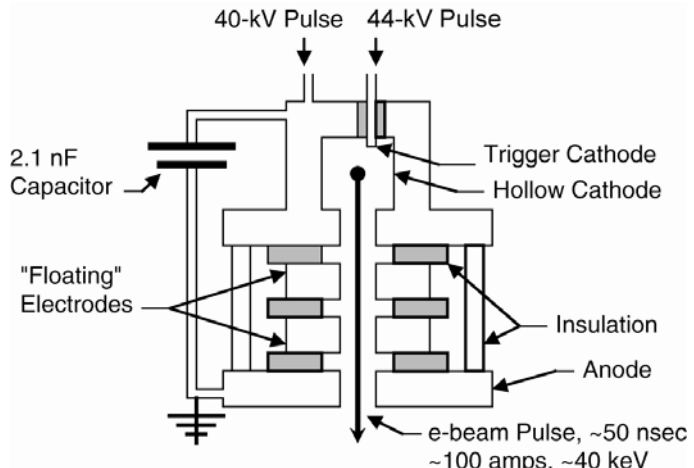


**Figure 4. Schematic of Pulsed E-Beam Gun.**

$$I = C_1 n / (1 + C_2 n) \quad (3)$$

Figure 5 shows schematically the relationship between  $I$  and  $n$  for continuous e-beam excitation. Typical values for  $C_2$  place the turning point (the point where the  $I$ - $n$  relationship can no longer be considered linear for any further increase in  $n$ ) at  $\sim 10^{16} \text{ cm}^{-3}$ .

For pulsed e-beam excitation, the various processes (excitation, fluorescence, quenching, and detection) are no longer constant in time; rather, they have some characteristic time scale associated with them. The quenching time scale,  $t_Q$ , is inversely related to  $n$ . If the excitation time and the detection time are short compared to  $t_Q$ , and if the detection time occurs soon after the excited state begins to be populated, then the effects of collisional quenching can be minimized.<sup>7</sup> This advantage comes at the expense of a great reduction in signal strength because since the fluorescence time scale is long compared to that of  $t_Q$ , a short detection time prevents detection of the entire fluorescence signal. If the "tail" of the fluorescence signal were measured along with the "head," the effects of quenching would become prevalent in the total accumulated fluorescence signal. Figure 6 shows a schematic of the time history of the e-beam pulse, the resulting fluorescence (with and without quenching), and the detection time. The increase in density, for which the  $I$ - $n$  relationship still remains valid, realistically increases by two orders of magnitude for detection time scales on the order of 20 nsec. Thus 0.1-atm flows (for 300 K) can be examined with a "linear" e-beam system.

Figure 7 shows the relationship between the (0-0) band emission strength and the density of air for three different choices of detector integration times: 10, 100, or 1000 nsec. Assumptions used in the calculations include the following characteristics for the e-beam: 100 amps in current strength, 100 nsec in duration, and a circular cross section with a 5-mm diameter. The curve for a 1,000-nsec detector integration time shows a linear relationship exists up to a density of approximately  $1.5 \times 10^{17} \text{ molecules/cm}^3$  (with the limit shown by the dashed vertical line), and the 10-nsec curve shows a linear relationship up to  $1.5 \times 10^{18} \text{ molecules/cm}^3$ .

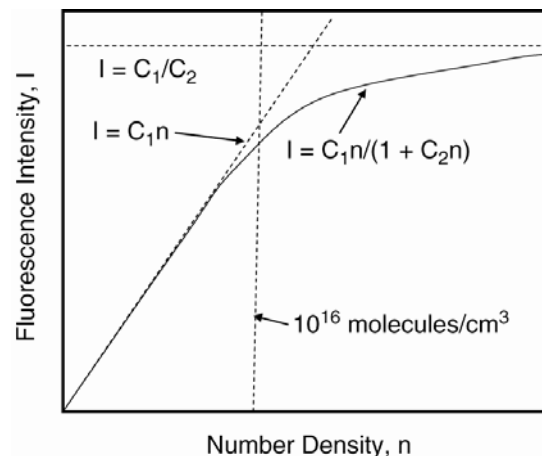


**Figure 5. Schematic of Signal Strength to Concentration Relationship for Continuous E-Beam Excitation.**

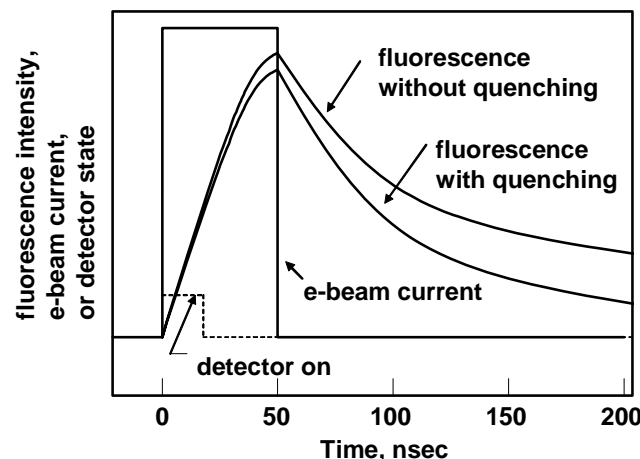


**Figure 6. Schematic of Temporal Features of Pulsed E-Beam System.**

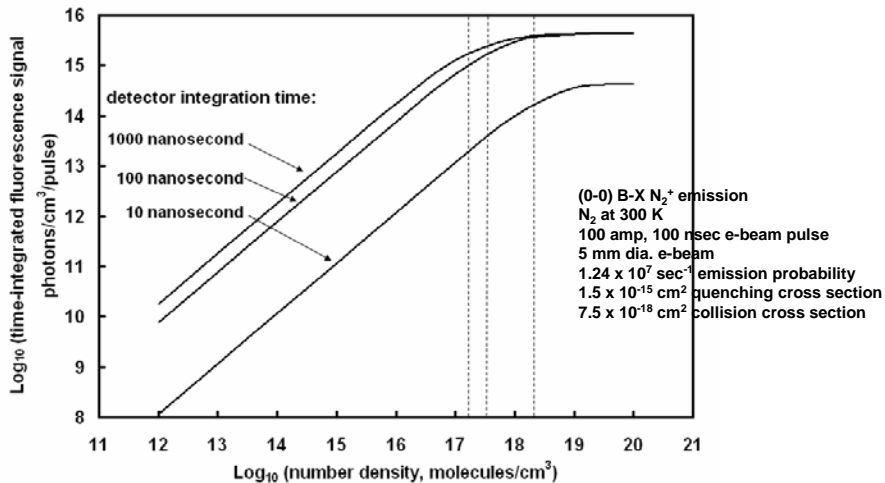


**Figure 7. Relationship Between (0-0)  $\text{N}_2^+$  Emission Band Strength and  $\text{N}_2$  Density for Three Different Detector Integration Times.**

Figure 8 shows a photograph of the AEDC pulsed e-beam system in operation. It is mounted on a 24-in.-diam glass vacuum chamber. For the photograph, the pulsed e-beam is discharging into the chamber while it is filled with 70 mtorr  $\text{N}_2$ . Obviously there is considerable light generated by the discharge of the pulsed e-beam gun. However, this represents the best-case situation for the gun's operation, where the gun discharges into a low-density medium and where there is no pressure barrier just downstream of the gun that can severely reduce the strength of the gun's electron discharge.

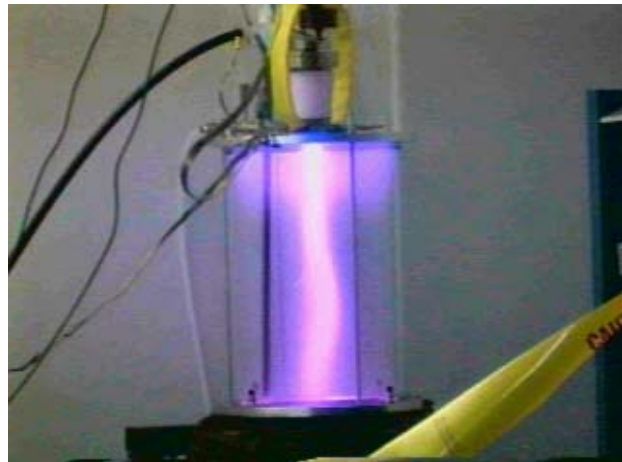


**Figure 8. Photograph of 27-kV Pulsed E-Beam Gun in Operation Using  $\text{N}_2$  at 70 mtorr.**

#### 4.0 APPLICATION OF PULSED E-BEAM GUN TO HIGH-PRESSURE FLOWS

Since the pulsed e-beam gun operates on the low-pressure side of the Paschen curve minimum, it is essentially limited to a maximum operational pressure of approximately 200 millitorr. However, most flows of interest for scramjet applications are much higher in pressure, usually of the order of tens of torr, corresponding to atmospheric pressures within the flight envelope of scramjet-powered flight vehicles. Because of the pressure disparity between measured flow and measuring device, there must be some kind of pressure separation barrier between the pulsed e-beam gun and the hypersonic test facility.

Three kinds of pressure separation methods were examined in this work: 1) thin beryllium foil, 2) differential pressure pump, and 3) fast acting rotary valve.

A thin foil of beryllium, the lightest metal, has been used as a pressure barrier for e-beam systems.<sup>12</sup> A 50- $\mu\text{m}$  thick foil was placed at the outlet of the pulsed e-beam gun inside the static

cell that is shown in Fig. 8. The gun was then fired, but no fluorescence was discernable by eye past the foil. This is somewhat to be expected because the energy of the electrons is, at most, 40 keV. Beryllium foils can be expected to absorb at least 30 keV of energy from the electrons,<sup>12</sup> so this barrier method is probably not appropriate for the relatively low-voltage pulsed e-beam gun. However, Ref. 12 does describe a promising new barrier made from Si N that does not absorb as high a percentage of energy. Nevertheless, the current technology of beryllium foils is not appropriate for pulsed e-beam pressure separation.

The second pressure separation method uses a differential pressure "pump" which is one or more orifices in series that inhibit gas flow. Figure 2 shows a two-stage differential pressure pump used in the past at AEDC for continuous e-beam work. Another differential pressure pump, specifically for the pulsed e-beam gun, has been developed at AEDC that can be configured for single-stage or two-stage operation. Figure 9 shows the schematics of the differential pressure pump used at AEDC, with each schematic for one particular arrangement of the orifices inside the pump unit. The pump has two removable orifices so that four different combinations of orifices can be assembled, as shown in the four schematics of Fig. 9. A packaged vacuum system consisting of a Roots blower backed by a vane pump, with a rating of 140 cfm @ 100 mtorr, is used to evacuate the differential pressure pump unit. Figure 10 shows a photograph of the pulsed e-beam gun, differential pressure pump, and vacuum pump, all deployed around the Laboratory Shock Tunnel at AEDC. Figure 11 shows the performance of the differential pump using all four of its configurations. It can be seen that 1 torr is the approximate maximum pressure that can be withstood by the differential pressure pump while still providing an adequate operational pressure in the gun.

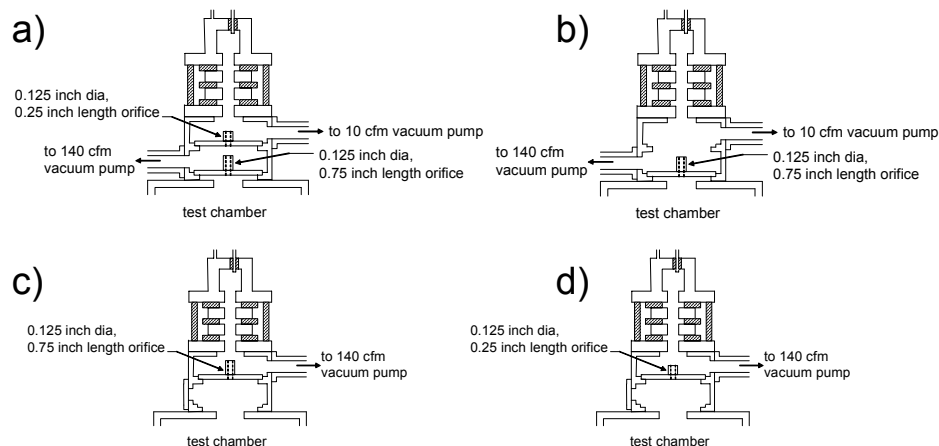


**Figure 9. Schematic of Differential Pressure Pump Configurations:**  
**a) Both Orifices Used, b) Long Orifice Used at Bottom, c) Long Orifice Used at Top, and d) Short Orifice Used at Top.**

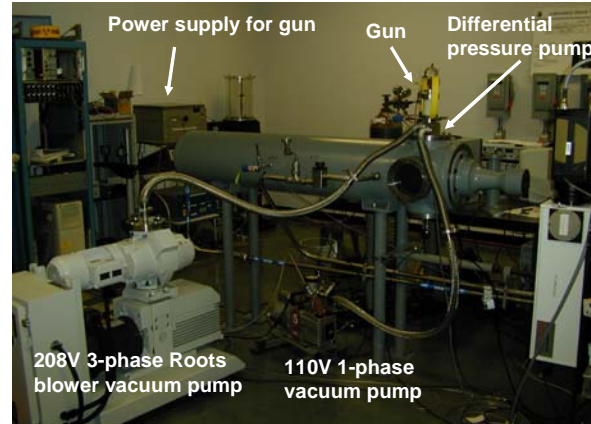
A 1-torr pressure separation is adequate for some applications of the pulsed e-beam system, such as the Mach 14 nozzle at Tunnel 9 which produces relatively low test cabin static pressures, but other applications, such as APTU, use much higher test cabin pressures of the order of tens of torr. For widespread application of the pulsed e-beam system, the third pressure separation method, a fast action valve, was developed.

The fast action valve concept has been demonstrated successfully at USC, and a description of the equipment can be found in Ref. 8. By opening the hole only for a short time before the pulsed e-beam gun fires, the pressure in the gun can be maintained at 70 mtorr by a relatively small vacuum pump. The Fast Action Rotary Valve Assembly (FARVA) has a 3-mm hole mounted in a rotating disk.

When a TTL trigger pulse is received by the valve motor, it accelerates the disk which rotates the hole into position within several milliseconds. The hole is positioned to allow the e-beam to pass through it (and to allow gas to enter the gun) for only a 150- $\mu$ sec duration. During this short time period the gun's pressure should not rise substantially above 70 mtorr.

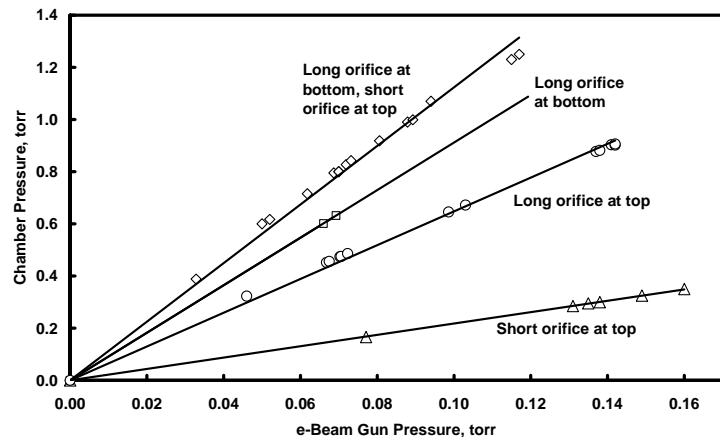
Figure 12 shows a conceptual drawing of the FARVA that shows the rotating metal blade under the FARVA. Figure 13 shows the peripheral equipment that is necessary for the proper timing of the valve and the pulsed e-beam gun, and Fig. 14 shows a photograph of the gun mounted on the AEDC Laboratory Shock Tunnel's dump tank. Figure 15 shows a wiring schematic for the four sets of wiring connections made to the programmable motor controller. In Fig. 13, the motor controller is connected to the high-torque motor and its position encoder. Using a computer connected via a USB port, one can program the controller to hold the rotary valve at a preset position until an external TTL-level trigger signal is received by the controller. The controller is programmed to send its maximum current to the motor, which causes the disk to accelerate and rotate into position. Once the disk is rotated into the position that opens up the pulsed e-beam pathway, another hole oppositely positioned on the valve disk is simultaneously opened that allows light from an LED to launch into an optical fiber. The fiber directs the light into a photomultiplier tube (PMT) whose voltage output is sent to a DG535 digital gate delay generator which shapes the PMT pulse into a TTL-level pulse that triggers the high-voltage power supplies of the pulsed e-beam gun. The high-voltage equipment only has approximately 5  $\mu$ sec of delay time, which is short in comparison to the approximately 150  $\mu$ sec that the e-beam path is opened. Thus there is no need to "pretrigger" the pulsed e-beam power supply before the beam path is opened. Figure 15 shows the wiring diagram for the connections between the motor, its controller, and the power supply that transforms 115-v AC power into 30-v DC power for the controller. A listing of the software code used by the motor controller software is given in Appendix I.

Figure 16 shows a graph of the typical firing sequence for the FARVA. The operation first involves setting the hole in the valve disk to a position about 28 deg before the open position. This is so that the valve disk will accelerate to a fast velocity by the time the e-beam path is opened. When the command is received by the motor controller to open the valve, there is approximately a 3 millisecond delay in the controller before it sends out a high-current signal to the motor. Figure 16 shows that even though a current of 25 amps is commanded to the motor controller, it can only send



**Figure 10. Photograph of Pulsed E-Beam System Located at AEDC Laboratory Shock Tunnel.**

made to the programmable motor to the high-torque motor and its position encoder. Using a computer connected via a USB port, one can program the controller to hold the rotary valve at a preset position until an external TTL-level trigger signal is received by the controller. The controller is programmed to send its maximum current to the motor, which causes the disk to accelerate and rotate into position. Once the disk is rotated into the position that opens up the pulsed e-beam pathway, another hole oppositely positioned on the valve disk is simultaneously opened that allows light from an LED to launch into an optical fiber. The fiber directs the light into a photomultiplier tube (PMT) whose voltage output is sent to a DG535 digital gate delay generator which shapes the PMT pulse into a TTL-level pulse that triggers the high-voltage power supplies of the pulsed e-beam gun. The high-voltage equipment only has approximately 5  $\mu$ sec of delay time, which is short in comparison to the approximately 150  $\mu$ sec that the e-beam path is opened. Thus there is no need to "pretrigger" the pulsed e-beam power supply before the beam path is opened. Figure 15 shows the wiring diagram for the connections between the motor, its controller, and the power supply that transforms 115-v AC power into 30-v DC power for the controller. A listing of the software code used by the motor controller software is given in Appendix I.



**Figure 11. Performance of Differential Pressure Pump Using 140-cfm Roots Blower Vacuum Pump.**

out a maximum of approximately 21 amps for a short duration, and then the back emf reduces the current sent by the controller. The controller sends angular position and velocity information to the computer via the USB connection. Interestingly, the velocity data sent by the controller do not match the velocity data derived from its position information. Both velocities are shown in Fig. 16, and generally the velocity data directly from the motor controller lag by about 3 milliseconds the velocity data calculated from the controller's position data. It is unclear which is the more reliable velocity data, but the motor controller's velocity data are arbitrarily chosen. Figure 16 shows these data have a relative maximum around 1.2 milliseconds after the controller is started. While almost twice the angular velocity could be achieved by waiting for the absolute maximum to occur, it was decided to accept the relative maximum of 25 revolutions per second in order to fire the pulsed e-beam gun at 12 milliseconds after the valve starts. This allows the gun to be used in transient facilities, such as the AEDC Laboratory Shock Tunnel.

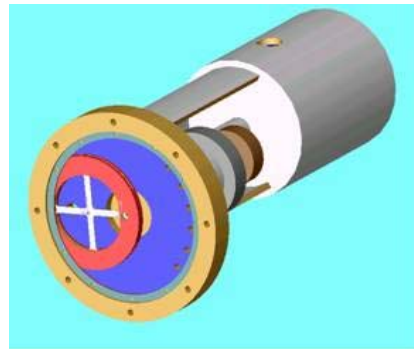


**Figure 12. Conceptual Drawing of FARVA Showing Rotating Disk at Bottom.**

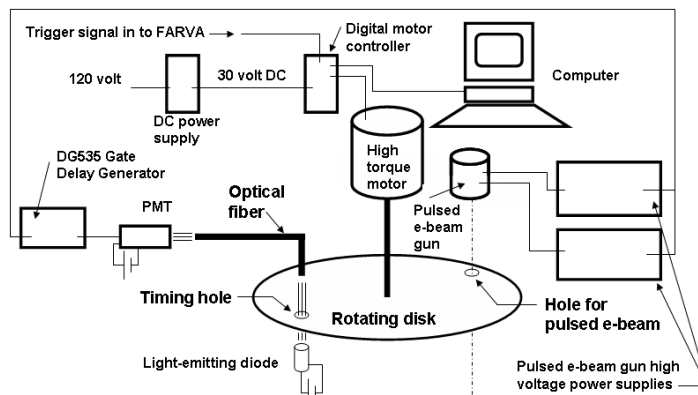


**Figure 13. Schematic of Equipment Used for Timing of FARVA and Pulsed E-Beam Gun.**

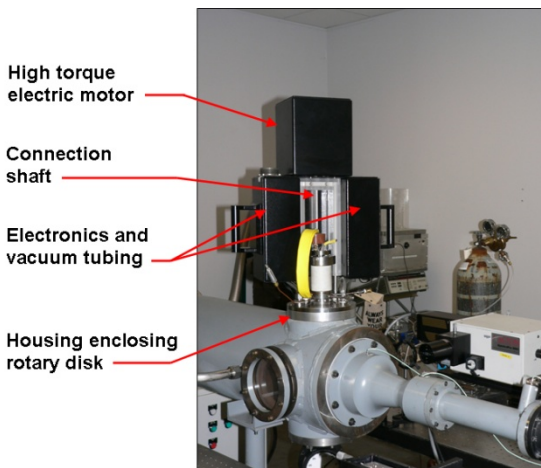
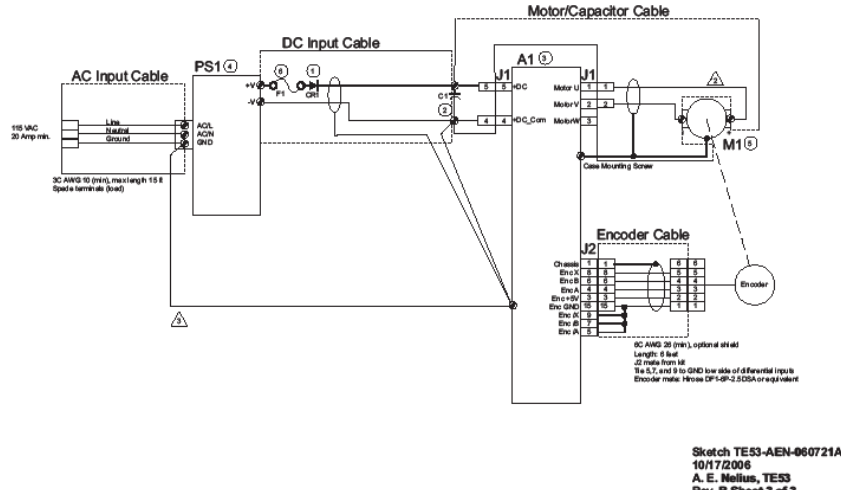


**Figure 14. Photograph Showing Placement of FARVA and Pulsed E-Beam Gun on Dump Tank of AEDC Shock Tunnel.**

**Schematic: FARVA Power Assembly, AccelNET, 115 VAC pwr**

1. Charge no. 03546064B4  
 ▲ Motor Phase Cable: min. 18 AWG, length 6 ft., twisted  
 ▲ Ensure Facility, PS1, A1, and M1 are securely grounded

① Pacificat 100 SPK 40A surge, Salmon TBA10/0L  
 ② Capacitor, 200V/1000μF, Cornell Dubilier C0810212001MC  
 ③ Servoamplifier, Copley Controls AccelNet ACP-090-3E  
 ④ Power Supply, Switching, Mean Well PSP-1900-27  
 ⑤ Motor, Moving Coil w/ Encoder, Whirlwind Inc. WY140-01-01IE  
 ⑥ Pulse, 1-Verm4, 16Amp



Sketch TE53-AEN-060721A  
 10/17/2006  
 A. E. Nellis, TESS  
 Rev. B Sheet 3 of 3

**Figure 15. Wiring Schematic for FARVA Programmable Motor Controller.**

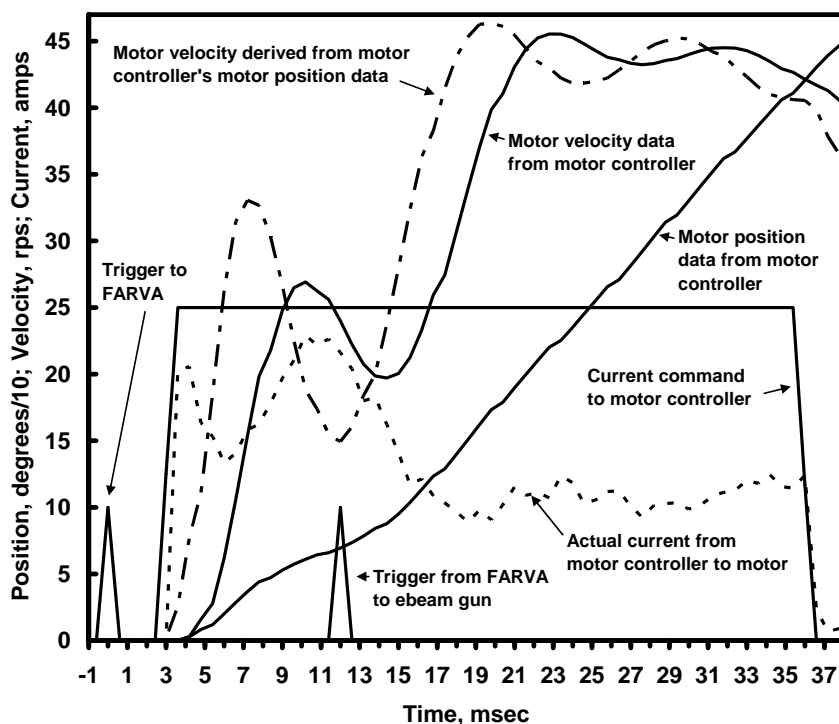


**Figure 16. Time History of FARVA Valve with 28 Deg ‘Windup.’**

The FARVA and pulsed e-beam gun were operated together on the static cell shown in Fig. 8. The gun was successfully fired into the static cell at pressures up to 50 torr of N<sub>2</sub>. At this pressure or below, there was sufficient fluorescence to be detected by eye. At 60 torr this fluorescence became extremely dim, and at 70 torr the system was fired 15 times with no

discernable fluorescence created. The 50-torr limitation is probably due to the rapid pressurization of the pulsed e-beam gun during the 150  $\mu$ sec of opening time for the FARVA.

## 5.0 DENSITY MEASUREMENT WITH THE PULSED E-BEAM TECHNIQUE

As mentioned in Sections II and III, a major reason for using a pulsed e-beam system rather than a conventional continuous e-beam system is that the short duration of the excitation process, along with short detection times, theoretically allows a significant increase in the linear range of the technique.

To verify these numerical findings, an experimental effort was performed where the pulsed e-beam gun was mounted on the Laboratory Shock Tunnel and its dump tank was pressurized with room temperature air. Rather than using a Faraday cup to measure e-beam current, a Pearson current coil was placed around the outlet of the pulsed e-beam gun to measure its discharge current. The time-integrated current measurement obtained from the Pearson coil is proportional to the total amount of electrons emitted from the pulsed e-beam gun for one pulse. By dividing the total amount of  $N_2^+$  fluorescence measured (during one entire e-beam pulse and for all wavelengths) by the time-integrated Pearson coil signal, the fluorescence measurement is "normalized" to account for changes in e-beam pulse strength. Figure 17 shows a graph of the measured (0-0)  $N_2^+$  emission band strength, normalized to the e-beam current, as a function of air density for air at 300 K. The detector time used for these data was 30 nanoseconds. Figure 7 shows that for this detector duration there should be a linear relationship between signal and density up to at least  $5 \times 10^{17}$  molecules/cm<sup>3</sup>, after which the signal strength rolls over and becomes insensitive to density changes. However, the experimental data in Figure 17 show no systematic increase in the signal with an increase in density from approximately  $1 \times 10^{16}$  to  $4 \times 10^{16}$  molecules/cm<sup>3</sup>. The explanation for this is possibly that as density increases, the spray of electrons increases in cross-sectional area so that there are fewer electrons at the measured sample volume location as density increases. This reduction in exciting electrons offsets the increase in  $N_2$  molecules so that there is no significant change in the signal strength as a function of air density. The spreading of the pulsed e-beam can be seen by eye in a darkened lab because of several  $N_2^+$  and  $N_2$  emission bands located in the violet and blue regions of the visible spectrum. Unfortunately, there are no magnetic focusing coils in the pulsed e-beam system with which to adjust the cross-sectional area of the emitted beam.

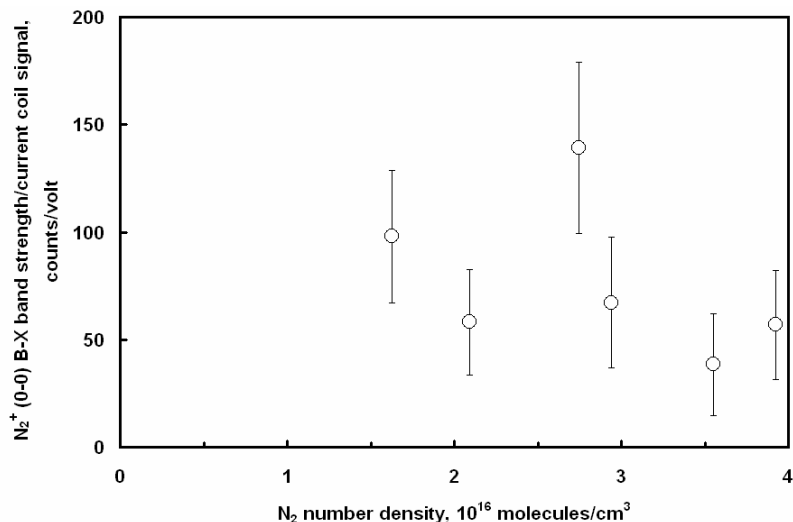


Figure 17. Experimental Relationship Between (0-0)  $N_2^+$  Emission Band Strength and  $N_2$  Density for 30-nsec Detector Integration Times.

The disappointing results shown in Figure 1–7 indicate that, notwithstanding the expected theoretical linear relationship, the pulsed e-beam technique cannot be used for density measurement, at least in the density range around  $10^{16}$  molecules/cm<sup>3</sup>. More extensive testing is necessary to determine the cause of this unexpected result.

## 6.0 PULSED E-BEAM N<sub>2</sub><sup>+</sup> EMISSION SPECTRA FOR TEMPERATURE MEASUREMENT

To demonstrate how temperature affects the shape of an N<sub>2</sub><sup>+</sup> spectrum created by pulsed e-beam excitation, Fig. 18 shows two N<sub>2</sub><sup>+</sup> theoretical spectra, one for 300 K and one for 2,000 K. The low-temperature spectrum shows that only a few rotational levels are significantly populated and contribute to the band emission, whereas at high temperature many rotational levels contribute. By comparing an experimental spectrum to a family of these theoretical spectra, and choosing the best-fit member of that family, a temperature measurement is obtained.

Figure 19 shows a representative experimental spectrum taken from 70 mtorr nitrogen gas during its excitation by the pulsed e-beam. A 0.5-m spectrograph with a 3,600 groove/mm grating was used to disperse the N<sub>2</sub><sup>+</sup> spectrum onto a 1-in.-wide gated, intensified CCD detector. In addition to the experimental spectrum, Fig. 19 shows a calculated N<sub>2</sub><sup>+</sup> spectrum whose shape is compared to the experimental spectrum. This calculated spectrum was created from an in-house AEDC software code. By comparing the shapes of the calculated and experimental spectra, one can deduce the rotational and vibrational temperatures of the N<sub>2</sub><sup>+</sup> since spectral shape is very much dependent on temperature. For example, as rotational temperature increases, the spectrum becomes broader due to the increasing population of rotationally and/or vibrationally excited states, which have emission wavelengths different from “low-temperature” states.

Both the rotational and vibrational temperatures can be measured simultaneously using the N<sub>2</sub><sup>+</sup> fluorescence from e-beam excitation. The ability to measure these two temperatures simultaneously can aid in understanding non equilibrium phenomena occurring in supersonic and hypersonic test facilities.<sup>12–14</sup> Figure 20 shows four simulations of the N<sub>2</sub><sup>+</sup> (0-0) and (1-1) emission bands, with each simulation for a different choice of vibrational temperature, T<sub>v</sub>, and rotational temperature, T<sub>r</sub>. For Fig. 20 the detector resolution is assumed to be 0.25 nm, rather than the 0.05-nm resolution shown in Figs. 18 and 19. For Figure 20a both T<sub>v</sub> and T<sub>r</sub> are 300 K, so this shows the expected relative strengths of the (1-1) and (0-0) bands at room temperature. The important thing to notice in Figure 20a is that there is a detectable (1-1) emission band, even though the ambient N<sub>2</sub> population has a negligible vibrationally excited

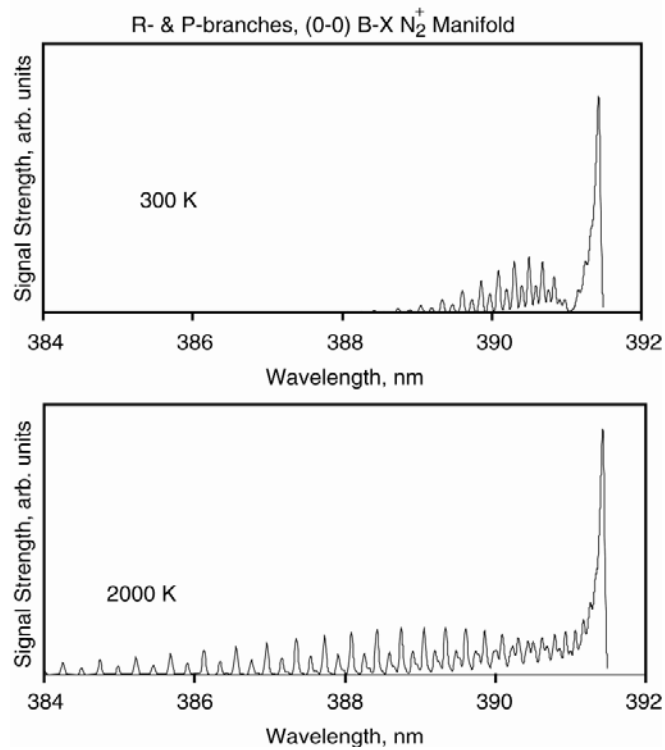


**Figure 18. Calculated N<sub>2</sub><sup>+</sup> (0-0) Emission Spectra at 300 and 2,000 K (Instrumental Width: 0.05 nm).**

population. This is because there is a small transition probability for  $N_2$  neutral molecules to be excited to the vibrationally excited  $N_2^+$  level. However, if a high-temperature population of  $N_2$  neutral molecules is examined, the amount of (1-1)  $N_2^+$  emission is much more than at 300 K because for  $N_2$  neutral to  $N_2^+$  excitation the (1-1) transition is much stronger than the (1-0) transition. This is why in Fig. 20b, which is for 1,900 K, the (1-1) emission band is stronger in comparison to the (0-0) band than for Fig. 20a. At high temperatures as in Fig. 20b there are many rotational emission lines that appear, which causes an overlap of the "high-temperature" part of the (0-0) band with the (1-1) band. The 1,900 K temperature is chosen because it is approximately the highest temperature that can be realistically obtained in the stagnation chamber of a hypersonic test facility. Thus Fig. 20b represents what might be obtained from the pulsed e-beam system if it were used in the high-temperature (but high-pressure) stagnation chamber. As that flow expands to hypersonic Mach numbers, the gas cools to extremely low temperatures, so for Fig. 20c a gas temperature of 100 K is used for both  $T_v$  and  $T_r$ . Even at this extremely low temperature there is still a small (1-1) emission band, again not because of any significant amount of vibrationally excited  $N_2$ , but because of the finite transition probability of the (1-0)  $N_2$  to  $N_2^+$  excitation transition. Lastly, Fig. 20d shows a simulated spectrum for a nonequilibrium flow at  $T_v = 1,900$  K and  $T_r = 100$  K. The (1-1) vibrational band is seen quite distinctly apart from the (0-0) band.

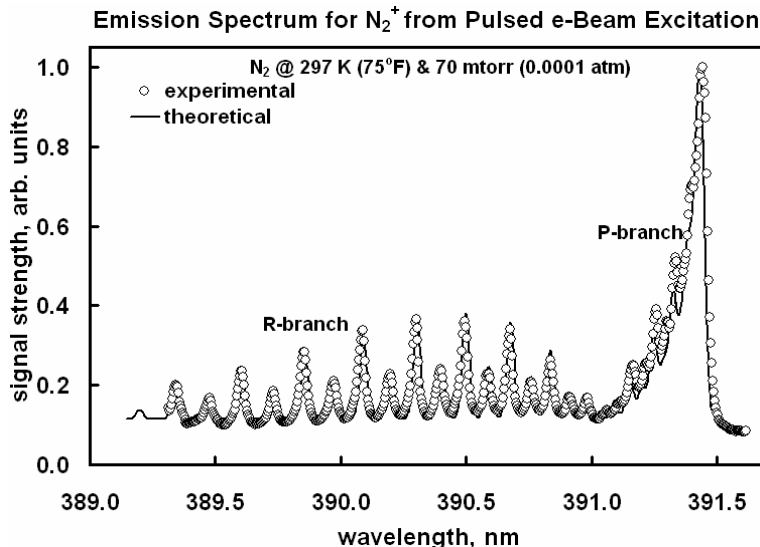


**Figure 19. Experimental  $N_2^+$  Emission Spectrum Compared to Theoretical Spectrum at 297 K.**

appear, which causes an overlap of the "high-temperature" part of the (0-0) band with the (1-1) band. The 1,900 K temperature is chosen because it is approximately the highest temperature that can be realistically obtained in the stagnation chamber of a hypersonic test facility. Thus Fig. 20b represents what might be obtained from the pulsed e-beam system if it were used in the high-temperature (but high-pressure) stagnation chamber. As that flow expands to hypersonic Mach numbers, the gas cools to extremely low temperatures, so for Fig. 20c a gas temperature of 100 K is used for both  $T_v$  and  $T_r$ . Even at this extremely low temperature there is still a small (1-1) emission band, again not because of any significant amount of vibrationally excited  $N_2$ , but because of the finite transition probability of the (1-0)  $N_2$  to  $N_2^+$  excitation transition. Lastly, Fig. 20d shows a simulated spectrum for a nonequilibrium flow at  $T_v = 1,900$  K and  $T_r = 100$  K. The (1-1) vibrational band is seen quite distinctly apart from the (0-0) band.

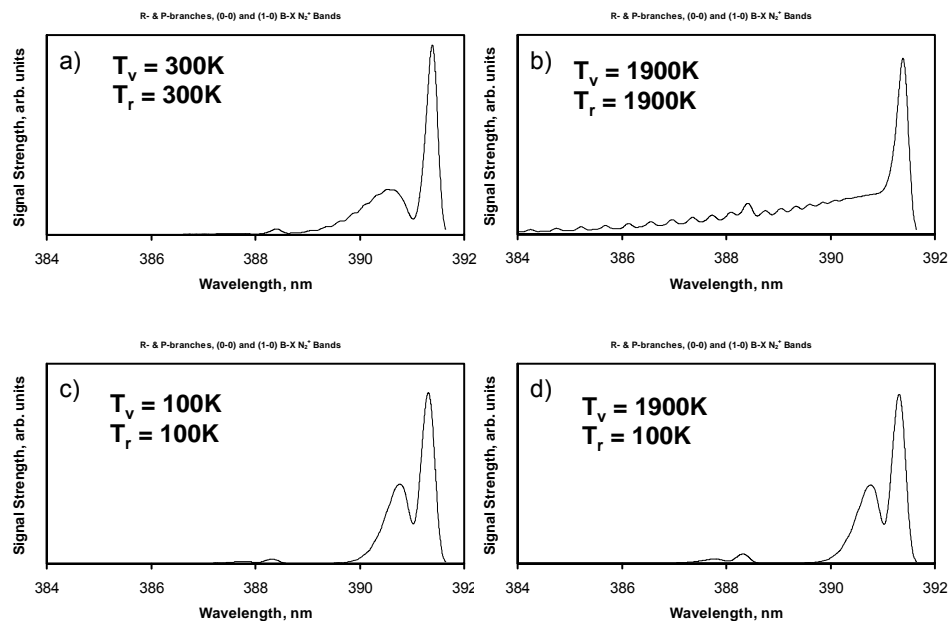


**Figure 20. Calculated  $N_2^+$  Emission Spectra at Four Combinations of Vibrational ( $T_v$ ), and Rotational ( $T_r$ ) Temperatures.**

Though it is hard to discern when comparing Figs. 20a and 20d, there is an increase in the ratio of the (1-1) band intensity to the (0-0) band intensity. Figure 21 shows how that ratio changes with vibrational temperature. At temperatures below approximately 700 K the ratio remains constant at  $\sim 0.025$ , which essentially is the ratio of the (1-0) and (0-0)  $N_2$  to  $N_2^+$  transition probabilities. The ratio approximately doubles from 700 K to 2,000 K, which is nominally the highest temperature that could be expected in electrically heated or combustion-heated hypersonic test facilities.

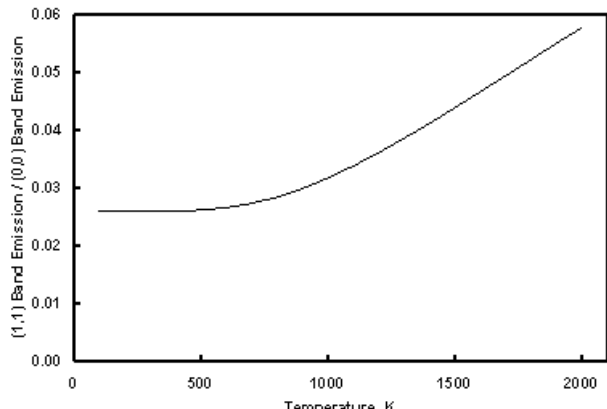


**Figure 21. Ratio of (1,1) to (0,0)  $N_2^+$  B-X Emission vs. Vibrational Temperature.**

## 7.0 APPLICATION OF PULSED E-BEAM SYSTEM TO HYPERSONIC FLOW

The flow at the nozzle exit for the AEDC Laboratory Shock Tunnel has been investigated using the pulsed e-beam gun, using either the differential pressure pump or the FARVA for pressure separation. The Laboratory Shock Tunnel, shown schematically in Fig. 22, has a conical nozzle with a 144 to 1 area ratio and produces a hypersonic flow with a Mach Number of approximately 7.5, assuming isentropic, ideal gas flow with constant specific heats. The hypersonic flow is initiated by bursting a diaphragm that separates low-pressure  $N_2$  from the high-pressure helium driver gas. Piezoelectric pressure transducers are located down the length of the driven gas section. They are labeled as K1, K2, etc., on Fig. 22.

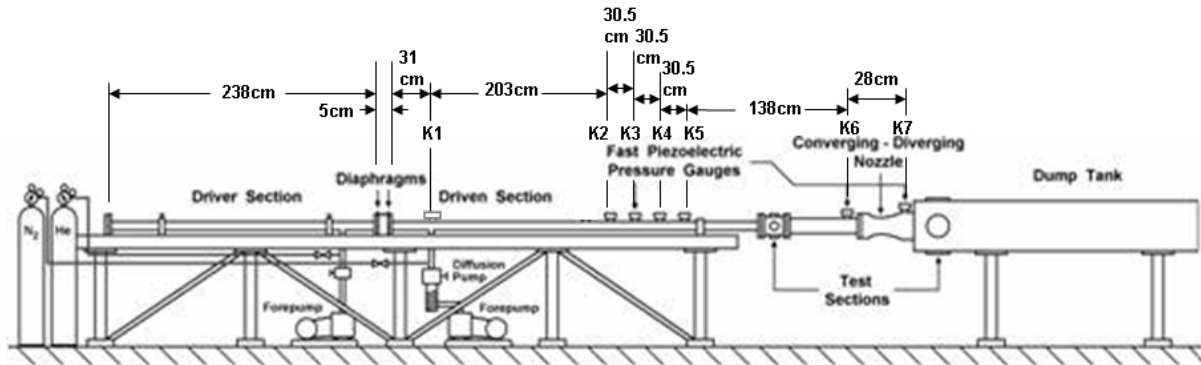


**Figure 22. Schematic of AEDC Laboratory Shock Tunnel.**

Figure 23 (a and b) shows the results of two shots of the pulsed ebeam gun at the nozzle exit. These two shots were obtained for two different firings of the shock tunnel, with both shots producing the same nominal static conditions at the nozzle exit: a dump tank pressure of 6.50 mtorr, and an expected static temperature of 640 K. However the stagnation temperature for this flow is expected to be several thousand degrees Fahrenheit, and the few milliseconds that the air is in the nozzle may be insufficient to allow complete vibrational relaxation. The existence of vibrational nonequilibrium is indeed noticed when comparing the  $N_2^+$  spectra of the two runs. Figure 23a shows the (0-0) and (1-1)  $N_2^+$  emission spectra, along with several  $N_2$  neutral emission spectra, for a time just 0.5 millisecond after the bursting of the diaphragm. The relative strengths of the (1-1) and (0-0) bands is essentially the same as that shown in Fig. 18 for a temperature of 300 K, which is the initial temperature of the undisturbed  $N_2$  in the dump

tank at the nozzle exit. For Figure 23b the delay time between the firing of the pulsed e-beam gun and the diaphragm bursting is 1.5 milliseconds. The additional delay of 1 millisecond over that of Figure 23a makes a significant difference in the flow examined. Figure 23b shows the co-presence of the helium driver gas along with the driven  $N_2$ . The helium presence is indicated by several isolated helium emission lines appearing across the entire spectrum of Figure 23b. More importantly, the  $(1-1) N_2^+$  emission band is much stronger in intensity than that of Fig. 23a. The strong  $(1-1)$  band strength in Fig. 23b shows that there is significant vibrational nonequilibrium existing in the flow that exits the conical nozzle. Unfortunately, because of the close proximity of the  $3^3P-2^3S$  He transition at 389 nm, it is hard to accurately measure the band strength of the  $N_2^+ (1-1)$  band in order to estimate the actual vibrational temperature at the exit.

To operate the pulsed e-beam gun at higher dump tank pressures, the differential pressure pump was replaced by the FARVA. For these tests the dump tank was pressurized up to an initial pressure of 10 torr of  $N_2$ . The driver section was pressurized with He at 850 psig. For these conditions the exit temperature is expected to be at least 420 K. Figure 24 shows the time history of the pressure at two locations in the shock tunnel and shows the time that the pulsed e-beam fires across the exhaust of the nozzle. One pressure trace is for K1, which is located just 31 cm from the diaphragm section. The increase in voltage produced by K1 when the shock passes by it is the trigger signal sent to the FARVA to begin its actuation. The second pressure trace is for K6, which is located 433 cm away from the K1 and approximately 35 cm away from the pulsed e-beam location. Comparing these two pressure traces shows the initial shock traveling downstream from the K1 to K6 location in the space of 3 milliseconds. The shock then reflects off the converging nozzle and travels upstream. Between the time the shock reflects and the pulsed e-beam gun fires, the pressure at the K6 location drops significantly. This is probably due to the loss of the driven gas as it exits through the nozzle into the dump tank. By the time the pulsed e-beam gun fires at 12.5 milliseconds, the K6 pressure has dropped to 150 psig from a high of 375 psig. As a result, it is unclear what the expected nozzle exit temperature should be when the pulsed e-beam gun fires.

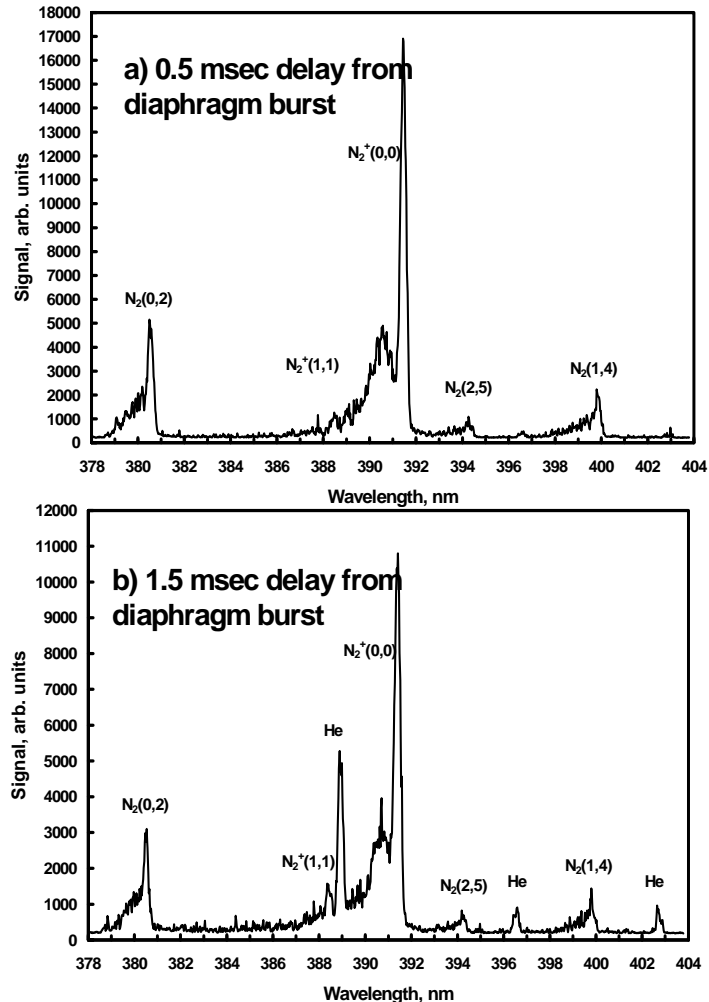


**Figure 23.  $N_2^+$  and  $N_2$  Neutral Spectra Obtained at Two Different Times after Bursting of Shock Tunnel Diaphragm.  $N_2$  Flow Conditions at Nozzle Exit: Mach Number = 7.5 and Exit Static Temperature = Approximately 700°F, Based on Ideal Shock Theory. Dump Tank Pressure 650 mtorr.**

The figure shows two sets of spectral plots, (a) and (b), illustrating the neutral spectra obtained at different times after the bursting of a shock tunnel diaphragm. The y-axis represents the signal in arbitrary units, and the x-axis represents wavelength in nanometers (nm), ranging from 378 to 404 nm. Plot (a) is for a 0.5 msec delay, and plot (b) is for a 1.5 msec delay. Both plots show several emission bands characteristic of nitrogen and helium. Key peaks labeled include  $N_2(0,2)$ ,  $N_2^+(1,1)$ ,  $N_2^+(0,0)$ ,  $N_2(2,5)$ ,  $N_2(1,4)$ , and He lines. The intensity of the  $N_2^+(1,1)$  band is significantly stronger in plot (b) compared to plot (a), indicating a more developed vibrational nonequilibrium in the 1.5 msec delay case. The He lines are also more prominent in plot (b).

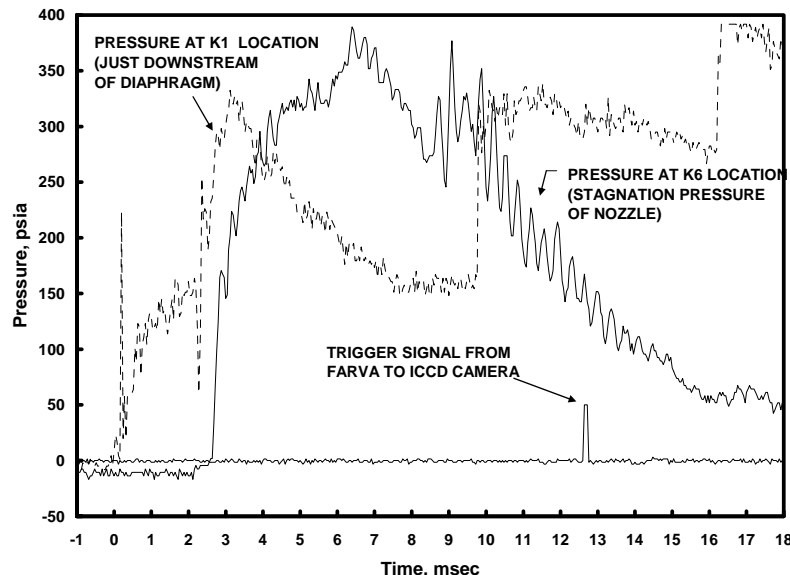


**Figure 24. Time History of Shock Tunnel Pressures at K1 and K6, Along with Signal from FARVA to Trigger ICCD and Pulsed E-Beam Gun.**

Figure 25 (a,b) shows two  $\text{N}_2^+$  spectra obtained from the shock tunnel while using the FARVA valve. The experimental data were obtained from a 0.5 m spectrograph, but an 1,800 groove/mm grating was used, so the effective instrumental linewidth is 0.5 nm. This is ten times the linewidth for the data of Figs. 18 and 19, which is why individual rotational lines are not resolved in Fig. 25a and 25b. An 1,800 groove/mm grating was used because it diffracts light more efficiently than the grating used for Figs. 18 and 19, thus allowing more light to be detected. Figure 25a is for the initial conditions in the dump tank, where the initial pressure is 10 torr and the temperature is 300 K. A comparison of the experimental data and theoretical data show relatively good agreement, but the noise in the signal associated with the weak signal creates random undulations in the experimental data that give the false impression of fine structure within the experimental spectrum. For Fig. 25b, the pulsed e-beam gun is fired into the hypersonic flow exiting the nozzle. The obvious difference between this spectrum and the previous one is that the shape of the Fig. 25b spectrum appears narrower. This is indicative of a colder temperature because fewer rotational levels are populated at cold temperatures. In fact, the theoretical spectrum shown in Fig. 25b is for an assumed temperature of 170 K. Rather than being colder, the hypersonic flow is expected to be hotter than room temperature, but vibrational nonequilibrium, heat transfer to the metal, and the great reduction in pressure all contribute to an inability to reliably predict what should be present at the nozzle exit when the pulsed e-beam gun fires.

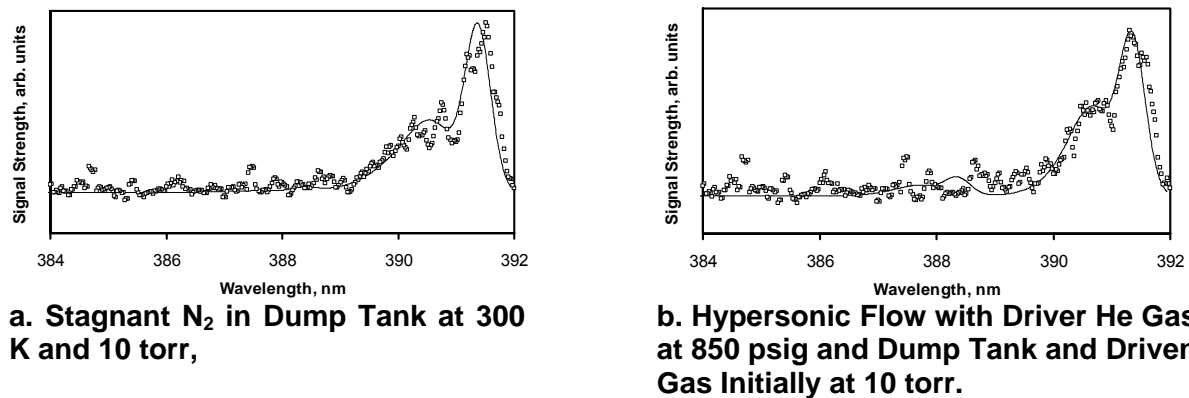


**Figure. 25. Pulsed E-Beam Spectra from AEDC Laboratory Shock Tunnel Using Spectrograph with 0.5-nm Resolution. Best-Fit Theoretical Spectrum is for 170 K.**

## 8.0 SUMMARY

A pulsed e-beam system has been assembled at AEDC with the intention of using it to measure vibrational and rotational temperatures simultaneously in hypersonic testing environments, as well as measuring the density of  $N_2$  simultaneously with the temperature measurements. The gun operates at internal pressures up to approximately 200 mtorr. While this is much higher than the internal pressures of continuous e-beam guns, it is still much lower than the pressures associated with hypersonic flows of current interest, which range from 1 to 100 torr for airbreathing scramjet propulsion. Thus to separate the low-pressure gun from hypersonic test media, a differential pressure pump has been developed for pressure separations up to approximately 1 torr. For higher pressures, a fast action rotary valve has been built. It has been demonstrated as allowing the gun to fire into room temperature gas at pressures up to 50 torr, when the valve allows a 150-microsecond opening time for the e-beam. It is possible that a shorter operating time may allow the gun to fire into even higher pressure test media. Nevertheless, the current 50-torr demonstration allows the gun to be applied to many hypersonic test situations. The fast action valve currently has a 12-millisecond delay between the time it receives a signal to open and the time it allows the pulsed e-beam to fire.

The original intention for the pulsed e-beam gun was to provide simultaneous measurement of  $N_2$  density and temperature. However, the relationship between the total  $N_2^+$  fluorescence emission and  $N_2$  density was determined to be nonlinear for densities from  $1 \times 10^{16}$  to  $4 \times 10^{16}$ . In fact, there was no systematic variation in the signal level detected in this density range. It is possible that the insensitivity of the signal to density change is due to a widening of the pulsed e-beam cross section with an increase in density, which counterbalances the expected signal increase due to density increase. In any case, this work has not found that the pulsed e-beam technique can be used for  $N_2$  density measurement. If the technique is used in the future for density measurement, then there will be a need for possible quenching corrections. To that end, the results of a literature review on quenching coefficients for  $N_2^+$  fluorescence are given in Appendix II of this report.

The pulsed e-beam system has been demonstrated on a hypersonic flow produced in a lab-scale shock tunnel at AEDC, where it detected significant vibrational nonequilibrium in the Mach 7.5 flow. This demonstration was for a 1-torr pressure in the test section of the shock tunnel. A single-stage differential pressure pump was used for the 1-torr pressure separation, which is approximately the maximum that it can produce when connected to a 140-cfm Roots blower/vacuum pump combination.

A second demonstration on a similar hypersonic flow produced in the same facility, but with a 10-torr initial pressure in the test section, was also performed. The pressure separation for this test was obtained with the fast action rotary valve. Comparisons of theoretical spectra with the experimental spectrum give an indicated temperature of 170 K. This is a surprising result since the expected temperature at the test location is expected to be significantly hotter than room temperature. The reasons for this low value of temperature measurement are unclear, but they could have something to do with vibrational nonequilibrium (vibrational energy not being transferred to rotational motion through the nozzle) and with lower initial temperatures than expected for the shocked flow entering the hypersonic nozzle.

Current plans are to transition the pulsed e-beam technique to a working, "production" hypersonic test facility to provide measurements of static rotational and vibrational temperatures nonintrusively. Future work to improve the performance of the pulsed e-beam system should include a reexamination of the solid material pressure separation technique. Beryllium was used for this project, but other materials – for example lithium and silicon nitride – are candidate materials. The ESTAR database maintained by NIST lists the e-beam interaction properties for several materials. Additionally, by using a higher energy e-beam, such as on the order of 100 keV or greater, a significant percentage of the beam can pass through beryllium or lithium.

## REFERENCES

1. Gochberg, L. A. "The Electron Beam Fluorescence Technique in Hypersonic Aerothermodynamics," AIAA Paper 94-2635, 1994.
2. Muntz, E. P. "The Electron Beam Fluorescence Technique." AGARDograph 132, 1968.
3. Williams, W. D., Hornkohl, J. O. and Lewis, J. W. L. "Electron Beam Probe for a Low Density Hypersonic Wind Tunnel." Arnold Engineering Development Center Technical Report AEDC-TR-71-61(AD-727004), 1971.
4. Limbaugh, C. C., Lewis, J. W. L., Kinslow, M., et al. "Condensation of Nitrogen in a Hypersonic Nozzle Flow Field." Arnold Engineering Development Center Technical Report AEDC-TR-74-31, 1974.
5. Cassady, P., Shelton, D., Price, L. L., Williams, W. D., and Powell, H. M. "Reacting Gas Experimental Data in Low Density Flow; Task VI. Electron Beam Density Measurement in Hypersonic Flow." Wright Laboratories Technical Report WL-TR-92-3045, 1992.
6. Lewis, J. W. L., and Williams, W. D. "Electron Beam Fluorescence Diagnostics of a Ternary Gas Mixture." AEDC-TR-73-96 (AD-762930), July 1973.
7. Lutfy, F. M. and Muntz, E. P. "Initial Experimental Study of Pulsed Electron Beam Fluorescence," *AIAA Journal*, Vol. 34, 1996, pp. 478-482.
8. Lutfy, F. M., Muntz, E. P. and Ketsdever, A. "Spectroscopic Survey of Xenon Using Pulsed Electron-Beam Fluorescence for Electric Thruster Diagnostics," AIAA Paper 2000-0605.
9. Christiansen, J. *The Properties of the Pseudospark Discharge Physics and Applications of Pseudosparks*. M. A. Gundersen and G. Schafer, Eds. Plenum Press, New York, 1990, pp. 1-13.
10. Williams, W. D., Sherouse, P. M., Crosswy, F. L., and Brandon, W. D. "AEDC Development of the Pulsed Electron Beam Fluorescence (PEBF) Technique for Hypersonic Test Facility Applications," AIAA Paper 02-5155, 2002.
11. Lutfy, F. M., and Muntz, E. P. "Spectroscopic Survey of Gases Found in Hypersonic Flows Using Pulsed Electron Beam Fluorescence," AIAA Paper 99-2452.
12. Miles, R. B., Macheret, S. O., and Schneider, M. N. "High Efficiency Nonequilibrium Air Plasmas Sustained By High Energy Electrons. Paper presented at 28<sup>th</sup> International Conference on Plasma Science (ICOPS 2001), Las Vegas, NV, 17-22 June 2001.
13. Boudreau, A. H. and Adams, J. C. "Characterization of Hypersonic Wind Tunnel Flow Fields," AIAA Paper 88-2006, 1988.
14. Sharma, S. P., Ruffin, S. M., Gillespie, W. D., and Meyer, S. A. "Vibrational Relaxation Measurements in an Expanding Flow Using Spontaneous Raman Scattering," *Journal of Thermophysics and Heat Transfer*, Vol. 7, 1993, pp. 697-703.

15. Smith, M. S. and Coblish, J. J. "Measurements to Assess the Degree of Thermal Nonequilibrium at AEDC Hypervelocity Wind Tunnel No. 9," AIAA Paper 2004-2399, 2004.
16. Price, L. L. and Lewis, J. W. L. "Collisional Quenching of Atomic and Molecular Nitrogen: I. Experimental Results," AEDC-TR-75-151, December 1975.
17. Mitchell. "Fluorescence Efficiencies and Collisional Deactivation Rates for N<sub>2</sub> & N<sub>2</sub><sup>+</sup> Bands Excited by Soft X-rays," *Journal of Chemical Physics*, Vol. 53, 1970, p. 1795.
18. Hirsh, Poss, and Eisner. "Absolute Fluorescence Yields of 3914 Angstrom Photons from N<sub>2</sub> and Air Excited by Relativistic Electrons," *Physical Review A*, Vol. 1, 1970, p. 1615.
19. Brocklehurst and Downing. "Mechanisms of Excitation of Luminescence in Nitrogen Gas by Fast Electrons," *Journal of Chemical Physics*, Vol. 46, 1967, p. 2976.
20. Brocklehurst. "Luminescence ... Part 1, Collisional Deactivation in Nitrogen," Transactions of the Faraday Society, 1964.
21. Lillicrap, "Collisional Quenching Effects in Nitrogen," NASA TMX-2842, 1973.
22. Smelley, "Reaction Rates for Collisional De-Excitation of the B Doublet Sigma (U)(+) State of N<sub>2</sub><sup>+</sup>," AD701670, 1969.
23. O'Neil and Davidson. "Fluorescence of Air and Nitrogen Excited by Energetic Electrons," AD673995, 1968.
24. Jolly and Plain. "Determination of Quenching Rates of N<sub>2</sub><sup>+</sup> by N<sub>2</sub> Using Laser-Induced Fluorescence," *Chemical Physics Letters*, Vol. 100, 1983, p. 425.
25. Johnson and Fowler. "Measured Lifetimes of Ritzation and Vibrational Levels of Electronic States of N<sub>2</sub>," *Journal of Chemical Physics*, Vol. 53, 1970, p. 65.
26. Chen et al. "Kinetic Studies of N<sub>2</sub> and N<sub>2</sub>-SF<sub>6</sub> Following Proton Excitation," *Journal of Chemical Physics*, Vol. 65, 1976, p. 3863.
27. Comes and Speier. "Optical Formation and Collisional Deactivation of First Negative System of Nitrogen," *Chemical Physics Letters*, Vol. 4, 1969, p. 13.
28. Tellinghuisen et al. "Quenching Rates for N<sub>2</sub><sup>+</sup>, Emission Bands Excited by 58.4 nm Irradiation of N<sub>2</sub>, N<sub>2</sub>O, and CO<sub>2</sub>," *Journal of Chemical Society Faraday Transactions 2*, Vol. 68, 1972, p. 833.
29. Mackay and March, "Collisional Deactivation Rates of N<sub>2</sub><sup>+</sup>," *Canadian Journal of Chemistry*, Vol. 49, 1971, p. 1268.
30. Belikov, Kusnetsov, and Sharafutdinov. "Rate of Collisional Quenching of N<sub>2</sub>O<sup>+</sup>, N<sub>2</sub><sup>+</sup> at Temperatures Less than 200K," *Journal of Chemical Physics*, Vol. 102, 1995, p. 2792.
31. Sukhinin, Khramov, and Sharafutdinov. "Measurement of Effective Cross Section of N<sub>2</sub> Sigma, v=0 Excited State of N<sub>2</sub><sup>+</sup> Ion Caused by N Moles at Temps 5-300 K," *Soviet Physics Technical Physics*, Vol. 26, 1981, p. 1022.

32. Pancheshnyi, et al. "Measurement of Rate Constants of N<sub>2</sub> and N<sub>2</sub><sup>+</sup>(B2Sigma+u,v'=0) Deactivation by N<sub>2</sub>, O<sub>2</sub>, H<sub>2</sub>, CO, and H<sub>2</sub>O in Nanosecond Discharge," Chemical Physics Letters, Vol. 294, 1998, p. 523.
33. Rothe and McCaa. "Emission Spectra of Molecular Gases Excited by 10keV Electrons," CAL Report Number 165, Cornell Aeronautical Laboratory, Inc., 1968.

## APPENDIX A. SOFTWARE FOR MOTOR CONTROLLER

```

CVM PROGRAM NAME=Homing Current Move.CCP
{
SEQUENCE NAME=HomeCLOSE/IN...
{
    HOME Next Index Negative      110rpm fast vel    22rpm slow vel      37 rps^2
    accel/decel 2872cts Offset YESWaituntilreferenced

    SET OUTPUT Output1 Hi

    WAIT FOR INPUT     Input IN6   Edge Trigger      Rising Active State

    CURRENT MOVE      25A current 100000000 mA/s current ramp
    NOwaitforatcommandedcurrent

    WAIT FOR DELAY TIME      25ms Delay Time

    CURRENT MOVE      0A current 100000000mA/s current ramp      YES
    waitforcommandedcurrent

    SET OUTPUT Output1 Lo
}

SEQUENCE NAME=Flip Outputs
{
    SET OUTPUT Output1 Hi

    WAIT FOR DELAY TIME      500ms Delay Time

    SET OUTPUT Output2 Hi

    WAIT FOR DELAY TIME      500ms Delay Time

    SET OUTPUT Output3 Hi

    WAIT FOR DELAY TIME      500ms Delay Time

    SET OUTPUT Output1 Lo

    WAIT FOR DELAY TIME      500ms Delay Time

    SET OUTPUT Output2 Lo

    WAIT FOR DELAY TIME      500ms Delay Time

    SET OUTPUT Output3 Lo

    WAIT FOR DELAY TIME      500ms Delay Time
}

SEQUENCE NAME=FastMove/Home
{
    CURRENT MOVE      25A current 100000000 mA/s current ramp
    NOwaitforatcommandedcurrent

    WAIT FOR DELAY TIME      30ms Delay Time
}

```

## APPENDIX B. REPORT ON COLLISIONAL QUENCHING LITERATURE REVIEW

Equation 3 in the main body of the report shows how the relationship between the e-beam fluorescence signal,  $I$ , and gas number density,  $n$ , becomes nonlinear if the value of  $C_2$  is significant. Whether  $C_2$  is significant depends on the relative strength of the spontaneous emission rate,  $A_T$ , to the collisional quenching rate  $k_i$ . The  $k_i$  value for  $N_2^+$  is known to be temperature-dependent as well as rotational-level dependent, so the proper modeling of  $k_i$  can be important as temperature changes and if temperature measurements based on the relative intensities of signals coming from the various rotational energy levels are made.

Because of the importance of collisional quenching on both density and temperature measurements derived from e-beam fluorescence, a study was commissioned as part of this project to assemble the quenching data for  $N_2^+$  that have been produced over the years. The following sections summarize the main results of this literature review study. First there is a description of the working equation that relates e-beam fluorescence to density, secondly there is a review of the quenching data used for density measurements, and thirdly there is a summary of the one work that presents rotational-level dependent quenching data.

### QUENCHING RATE-SIGNAL STRENGTH RELATIONSHIP

A current of electrons,  $a$ , passing through a gas will excite the gas to an electronically excited state at a rate given by:

$$\frac{dn_i}{dt} = n \frac{a}{A} \sigma \quad A1$$

where  $n_i$  is the number density of the gas at a specific energy level in the upper excited electronic energy level,  $n$  is the number density of the gas in its original unperturbed ground state,  $a$  is the current in electrons/sec,  $A$  is the cross-sectional area of the electron beam, and  $\sigma$  is the collision cross section for electron-molecule collisions that populate the molecule's  $i$ th energy level. However, the  $i$ th level population is also depleted by the spontaneous emission of light from level  $i$  to all allowable energy levels. To account for this depletion, the above equation is modified to:

$$\frac{dn_i}{dt} = n \frac{a}{A} \sigma - n_i A_T \quad A2$$

where  $A_T$  is the spontaneous emission probability for molecules in the  $i$ th level to spontaneously emit radiation and fall into any allowable energy level. The above equation can be further modified to account for radiationless depletion of the  $i$ th level by way of collisional quenching:

$$\frac{dn_i}{dt} = n \frac{a}{A} \sigma - n_i A_T - n_i \sum_j n_j k_{ij} \quad A3$$

where  $n_j$  is the number density of a particular gas species  $j$ , and  $k_{ij}$  is the collision rate constant for collisions between the gas species of interest in energy level  $i$  and another gas species  $j$  (in an unspecified energy level). Additional terms can be added to account for secondary electron excitation, diffusional and convective losses, etc., but these terms are ignored. See Reference

## APPENDIX B. CONTINUED

2 for their consideration s. For steady-state conditions where the increase in  $n_i$  is 0, the above equation can be rearranged into the following:

$$n_i = \frac{n \frac{a}{AA_T} \sigma}{\left( 1 + \frac{\sum n_j k_{ij}}{A_T} \right)} \quad A4$$

The above equation is in a form similar to that of Eq. (3) in the main body of this report, where the  $C_2n$  term in Eq. (3) is now represented by the ratio of the sum of the  $n_j k_{ij}$  terms to  $A_T$ . The measured fluorescence signal for a transition from energy level  $i$  to level  $k$ ,  $I_{ik}$  (in detected photons per second), is related to  $n_i$  by:

$$I_{ik} = \varepsilon \left( \frac{\Omega}{4\pi} \right) L A A_{ik} n_i = \frac{\varepsilon \left( \frac{\Omega}{4\pi} \right) L A_{ik} n \frac{a}{A_T} \sigma}{\left( 1 + \frac{\sum n_j k_{ij}}{A_T} \right)} \quad A5$$

where  $\varepsilon$  is the light detection efficiency of the measurement system,  $\Omega$  is the solid angle within which fluorescence is collected,  $L$  is the length of the electron beam that is detected, and  $A_{ik}$  is the spontaneous emission transition probability for a transition from energy level  $i$  in the electronically excited state to level  $k$  in the ground electronic state. The above equation is valid for steady-state situations only.

### ROTATIONAL LEVEL-DEPENDENT QUENCHING RATE DATA

Equations (A4) and (A5) suggest that a knowledge of the values of  $k_{ij}$  is needed to properly relate the measured fluorescence to a particular rotational level population  $n_i$  of  $N_2^+$ . However, a very thorough literature review revealed only one publication that measured rotational-level dependent values of  $k_{ij}$ , and this publication happened to be an AEDC Technical Report.<sup>16</sup> The report describes measured  $k_{ij}$  values for two temperatures only: 94 K and 300 K, and both are for nitrogen as the collider species. The two graphs from the TR for these two temperatures are shown in Fig. B-1. A comparison of these two graphs shows that in general the  $k_{iN_2}$  values are larger for the colder temperature than for the warmer. For example, for the 3<sup>rd</sup> rotational level, the  $k_{3,N_2}$  value is  $2.55 \times 10^{-10} \text{ cm}^3/\text{sec}$  at 300 K and rises to  $5.5 \times 10^{-10} \text{ cm}^3/\text{sec}$  at 94 K. More importantly, both graphs show that  $k_{iN_2}$  is a function of rotational level  $i$ . Values for  $k_{iN_2}$  vary by a factor of five for the 94 K case and by a factor of two for the 300 K case as the rotational level is varied from 1 to 11.

The drop in the quenching rate with increasing rotational level indicates that an experimentally obtained  $N_2^+$  emission spectrum will have its lower rotational level components appear weaker in comparison to its higher rotational level components, thus appearing "hotter" than if the quenching rates were independent of rotational level.

## APPENDIX B. CONTINUED

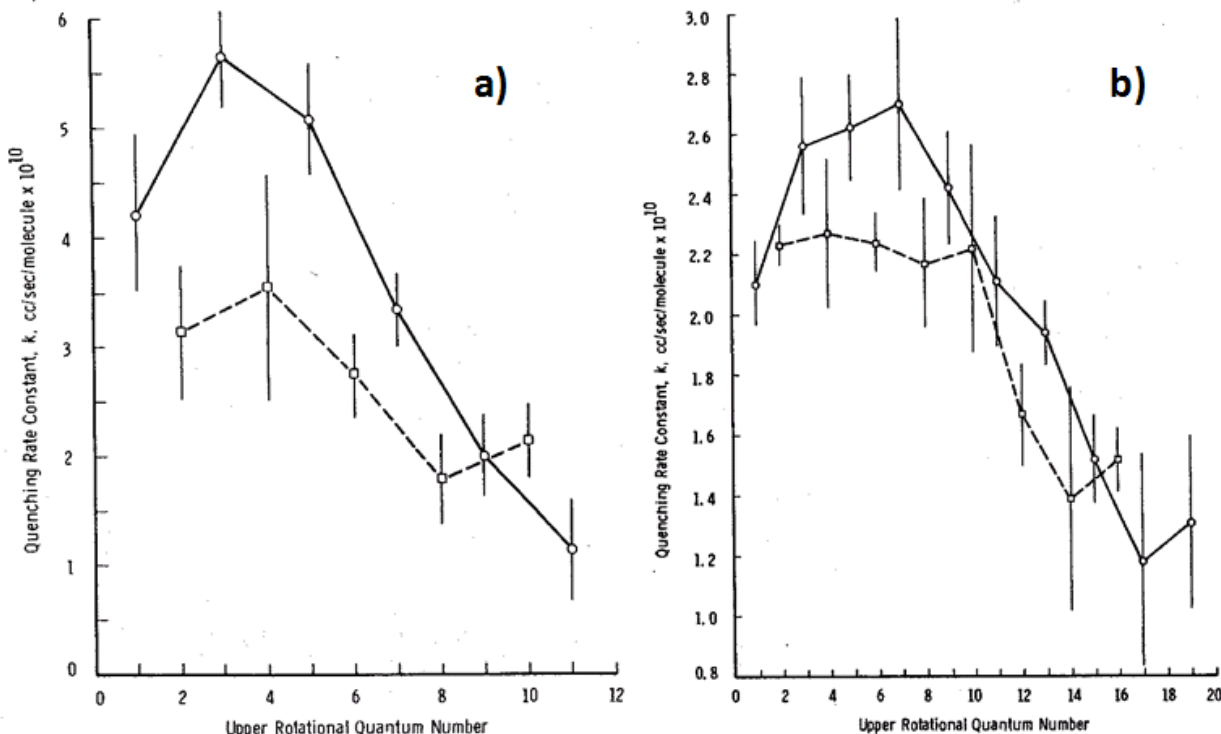


**Figure B-1. Graphs of Quenching Rate Coefficient  $k_{iN_2}$  Versus Rotational Energy Level  $i$  for  $N_2^+$  Collisions with  $N_2$  at Two Temperatures: a) 94 K, b) 300 K. Graphs Taken from Ref. 16.**

## ROTATIONAL LEVEL-INDEPENDENT QUENCHING DATA

Even though Ref. 16 is the only source of rotational level-dependent quenching data found in the literature review, there were several references that were found to contain quenching data that were not resolved into particular  $N_2^+$  rotational energy levels. These references were concerned with the quenching rate associated with the entire  $N_2^+$  (0-0) (B-X) emission band.

The  $N_2$  molecule has the most quenching data references. In addition to Ref. 16, these are Refs. 17 through 32. Figure B-2 shows a summary of the  $N_2$  quenching information obtained from those references. In this figure, the size of each data point is scaled to represent the relative confidence level or "data weight" of the  $k_{N_2}$  data for that particular point. Figure B-2 also displays a curve which is the best-fit curve to the weighted data. The equation for this best-fit curve is

$$k_{N_2} = 3.8 \times 10^{-10} + 28.317 \times 10^{-10} (T^{-0.75976}) \quad \text{A6}$$

where  $T$  is in kelvins and the units of  $k_{N_2}$  are  $\text{cm}^3/\text{sec}$ . At high temperatures the value of  $k_{N_2}$  approaches  $3.8 \times 10^{-10} \text{ cm}^3/\text{sec}$ , and for temperatures below about 200 K the value becomes significantly higher.

## APPENDIX B. CONCLUDED

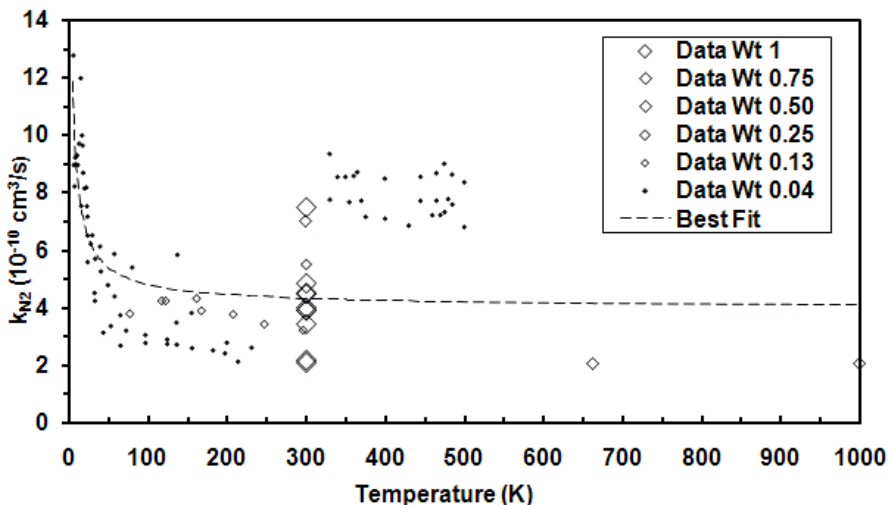


**Figure. B-2. Graph of Quenching Rate Coefficient  $k_{N_2}$  for Collisions Between B-State  $N_2^+$  and  $N_2$ . Data in Graph Obtained from Refs. 16 through 31.**

A literature review of quenching data for  $N_2^+$  colliding with other gas species was also made. However, the extent of the information is much less than for collisions with  $N_2$ . Table 1 shows quenching data for  $CO_2$ ,  $CO$ ,  $C_2H_6$ ,  $He$ ,  $O_2$ , and  $H_2O$ , along with the references from which the data were obtained. All of the data in Table B-1 is for a temperature of 300 K.

**Table B-1. Collisional Quenching Rates for B-state  $N_2^+$  Colliding with Species i. Data Obtained from References Listed in Right Column.**

Gas Species i	$k_i, 10^{-10} \text{ cm}^3/\text{sec}$	Reference Number
$C_2H_6$ 20		28
$He$ 0.3		28
$CO_2$ 16		28
$CO_2$ 16		33
$H_2O$ 8.6		28
$H_2O$ 9.4		33
$CO$ 1.9		32
$CO$ 3.5		28
$CO$ 9.4		33
$O_2$ 7.4		17
$O_2$ 7.1		18
$O_2$ 3.8		20
$O_2$ 9.3		23
$O_2$ 1	1	28
$O_2$ 5.1		32
$O_2$ 9.4		33

## APPENDIX C. IMPROVEMENTS TO PULSED E-BEAM SYSTEM

The work described in the previous sections of this report was accomplished under one HSHT focus area-funded project. After the end of the original project, a smaller follow-on project was initiated to address some of the operational issues that became apparent during the execution of the original project. Three main areas of system improvement were identified for this follow-on project. The first area of interest is associated with improving the strength and consistency of e-beam output. Output consistency is especially important when the pulsed e-beam system is applied to a transient test facility, where only one pulse from the system can be obtained during the test event. Repeated operation of the FARVA-equipped pulsed e-beam system has shown that there is a high degree of variability in the strength of the electron discharge from the gun, even though all experimental parameters are held constant. The second system improvement to be investigated is the decrease in the overall response time of the pulsed e-beam system. The system in its configuration at the end of the previously-funded TE/ST project has a 12 millisecond nominal delay time. When the pulsed e-beam system is applied to a transient facility, such as a shock tunnel, such a long time delay can be a major system limitation. The third system improvement to be investigated is the proper hole size for the aperture disk in the FARVA. As the system is configured at the end of the original project, there is a 0.125-in.-diameter aperture in the rotating disk of the FARVA. This aperture size may have been arbitrarily selected by the vendor who constructed the FARVA, and the optimum hole size could depend on the pressure of the test medium into which the gun discharges.

The following sections describe the work accomplished by the follow-on project for the three improvement areas mentioned above.

### **IMPROVEMENT 1: INCREASE IN STRENGTH AND RELIABILITY OF PULSED E-BEAM OUTPUT**

#### **Theory of Operation of Pulsed E-Beam High Voltage Electronic Equipment**

The pulsed e-beam system comprises three primary components: the e-beam gun, the high-voltage pulse generator, and the delayed trigger generator. The high-voltage pulse generator produces a 10-μsec charging pulse of a maximum of -40 kV to a cathode on the electron gun cathode. The delayed trigger generator produces a fast rise-time pulse of about -5 kV to a different electron gun cathode to initiate breakdown in the gun, which results in electron beam discharge. Figure 4 shows the cathode arrangement. The electron beam gun is a pseudo-spark electron beam generator.

The delayed trigger generator is similar to a radar pulse modulator or pulsed laser driver composed of a high-voltage power supply that charges a pulse forming network quickly discharged through a hydrogen thyratron switch into the primary of a step-up transformer. A limited number of off-the-shelf products performing the function of a thyratron drive for pulse switching were identified, but none met the specialized power and switching waveform requirements of the pulsed e-beam gun.

The high-voltage pulse generator is a pulsed power supply that generates its output similarly to the delayed trigger generator. Instead of a thyratron, a four-gang bank of slower, but more powerful, silicon controlled rectifiers is used to switch the pulse-forming network-stored charge through a step-up output transformer. The output transformer is contained in a transformer oil bath, creating extra maintenance and safety requirements.

## APPENDIX C. CONTINUED

Initial evaluation of the high-voltage pulse drive revealed the front-end low-voltage pulse delay board feeding the fast pulse-generating thyratron neither produced dc power nor generated pulses of any kind when external power was supplied. This indicated that the e-beam gun had been self-triggering randomly within the 10- $\mu$ sec-wide pulse generator signal instead of externally triggering precisely from the trigger generator in all prior operations.

An alternative to drive the next stage employed laboratory instruments to produce the required signals. The connection diagram is shown in Figure C-1.

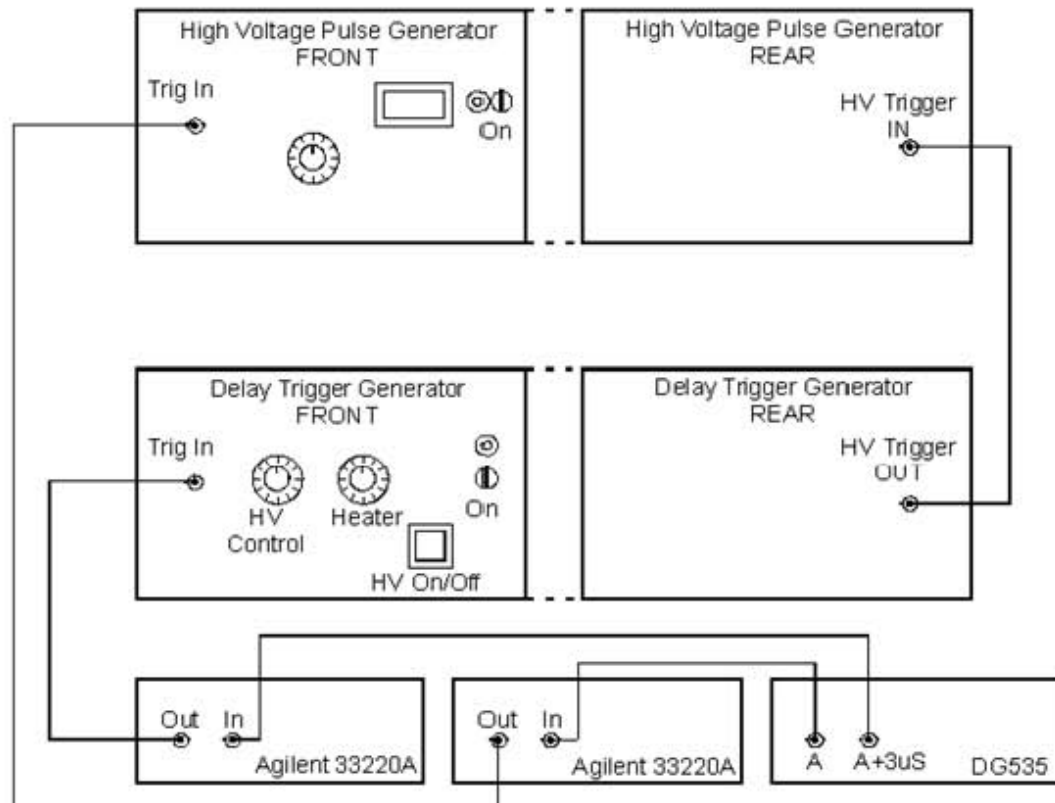


**Figure C-1. High-Voltage Pulse Generation Hook-Up.**

### Troubleshooting

After alleviating the trigger generator output problem, the system malfunctions observed were 1) no apparent transfer of the delay trigger generator output through the high-voltage pulse generator, 2) the high-voltage pulse generator output appeared to terminate prematurely, and 3) the Agilent 33220A's showed effects of the pulsing by "chirping" and intermittently blanking out after shots.

Two new transistor circuits for driving pairs of silicon control rectifier (SCR) gates harder and to provide higher upstream isolation were built, and the individual SCR gate interfaces were redesigned to provide additional upstream isolation and overvoltage protection. Figure C-2 illustrates the circuit modifications.

## APPENDIX C. CONTINUED

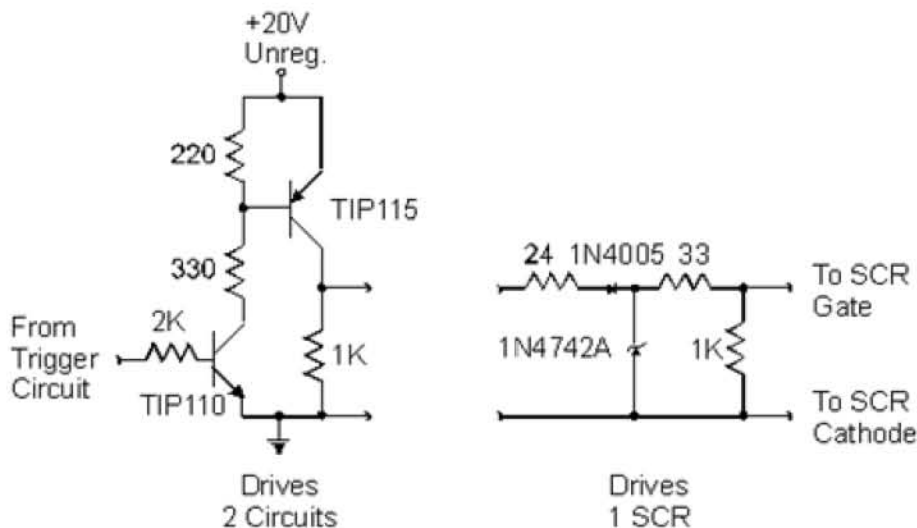


**Figure C-2. Pulse Generator Circuit Modifications. Circuit on Left Drives Two Circuits Shown on Right in Parallel.**

Technical personnel disassembled, inspected, and cleaned the pulsed e-beam gun to test the system from a known starting point. Figure C-3 shows components of the gun when apart. All interior gun surfaces including plates and spacers were cleaned with isopropyl alcohol before reassembling and vacuum pumping overnight to remove residuals from the cleaning process.



**Figure C-3. Pulsed Electron Gun Shown Disassembled.**

### High-Voltage Pulse Generator Problems

The pulse forming network current-limiting resistors were replaced with 2 each 25 k ohm 10 watt wirewound resistors. The high-voltage pulse generator was reassembled with critical component nodes accessible from the top of the chassis. The high-voltage pulse generator following rebuild employing these and other construction improvements facilitating troubleshooting and repair is shown in Fig. C-4.

## APPENDIX C. CONTINUED

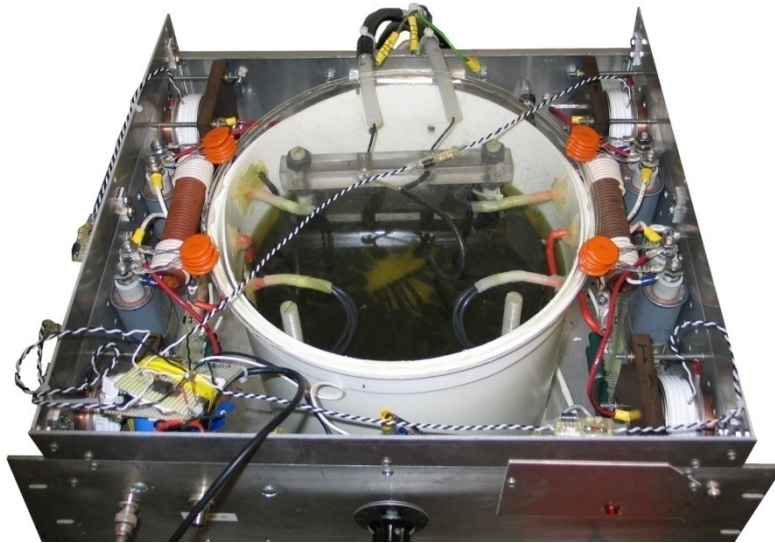


**Figure C-4. Pulse Generator Following Rebuild.**

### Testing of Overhauled Hardware

After the above-mentioned electro nic system improvements were made, the pulsed e-beam system was operated to determine the influence of the modification upon performance. The gun was remounted on the static cell that is shown in Fig. 8 of the original report. Various pressures in the gun and in the test medium in the static cell were produced. Figure C-5 shows a time history of the high voltages measured at the output of the high-voltage pulse generator and the delayed trigger generator for an internal pressure of 71.5 mtorr in the gun and 51 mtorr for the test medium. This graph shows that for this particular pulse the high voltage achieves a value of approximately -19 kilovolts when the delay trigger generator fires. Figure C-5 is for the installation of two storage capacitors on the pulsed e-beam gun, which raises the system capacitance from 1.5 nF to 3.2 nF. As a result of this extra capacitance, the time required to achieve a given voltage for the gun's cathode is increased. This is obvious when comparing Fig. C-5 to the traces of Fig. C-6, which were obtained from the modified pulsed e-beam system, except that only the one original 1.5 nF capacitor is used. For this situation it takes less time for the gun's cathode to achieve a given high voltage. In fact, a voltage of over 25 kilovolts is obtained before the delay pulse trigger arrives at the high-voltage pulse electronics. The electrical energy delivered to the gun by the dual-capacitor system is  $3.2 \text{ nF} \times 19 \text{ kV}^2 = 1.16$  joules, whereas the single-capacitor system delivers  $1.5 \times 26 \text{ kV}^2 = 1.0$  joules. However, the dual-capacitor system, because of its slower rate-of-increase in voltage, can be more accurately triggered by the delay pulse generator than can the single-capacitor system. For the two tests shown in Figs. C-5 and C-6, the delay time sent to the delay trigger generator is 3  $\mu\text{sec}$ . However, if the dual-capacitor system had received a longer trigger delay, on the order of 3.5  $\mu\text{sec}$ , then its maximum attainable voltage difference would be similar to the 25 kV obtained from the single-capacitor system. By doing this, the current that is discharged by the dual-capacitor pulsed e-beam gun should be increased from that of the single-capacitor gun by the ratio of capacitance,  $3.2/1.5 = 2.13$ , and the resulting electrical energy discharged by the pulsed e-beam gun should increase by the same ratio. Figure C-7 shows a photograph of the pulsed e-beam emitted by the pulsed e-beam gun using the dual-capacitor configuration along with the modified electronic circuits of the high-voltage pulser and the delay trigger generator. The output strength is visually similar to that of the original unmodified system, whose output is

## APPENDIX C. CONTINUED

photographed in Fig. 8 of the original report. The main result of all of the electrical system improvements has been the provision of more reliability and consistency in the output of the pulsed e-beam gun, rather than an increase in the voltage or energy that the gun provides.

### **Summary of Electrical Modifications to Pulsed E-Beam System**

Shown below is a listing of the electrical modifications made to the delay trigger generator, the high-voltage pulse generator, and the pulsed e-beam gun. All of these modifications together have improved the performance of the system (increased pulse-to-pulse reliability and consistency); however, not every modification may have resulted in a contribution to the system improvement.

1. Replaced faulty pulse-delay circuit from trigger generator with lab equipment (DG535 and 33220A)
2. Removed faulty front panel display and power circuit from pulse generator
3. Replaced all four pulse generator SCR trigger interface and isolation circuits with improved circuits
4. Cleaned pulsed e-beam gun internals
5. Removed superfluous electrolytic capacitors from pulse generator
6. Replaced all four faulty pulse generator pulse forming network current-limiting resistors
7. Reassembled pulse generator to provide troubleshooting access to components
8. Added 1.7 nF capacitor to existing 1.5 nF gun charging capacitor

## APPENDIX C. CONTINUED

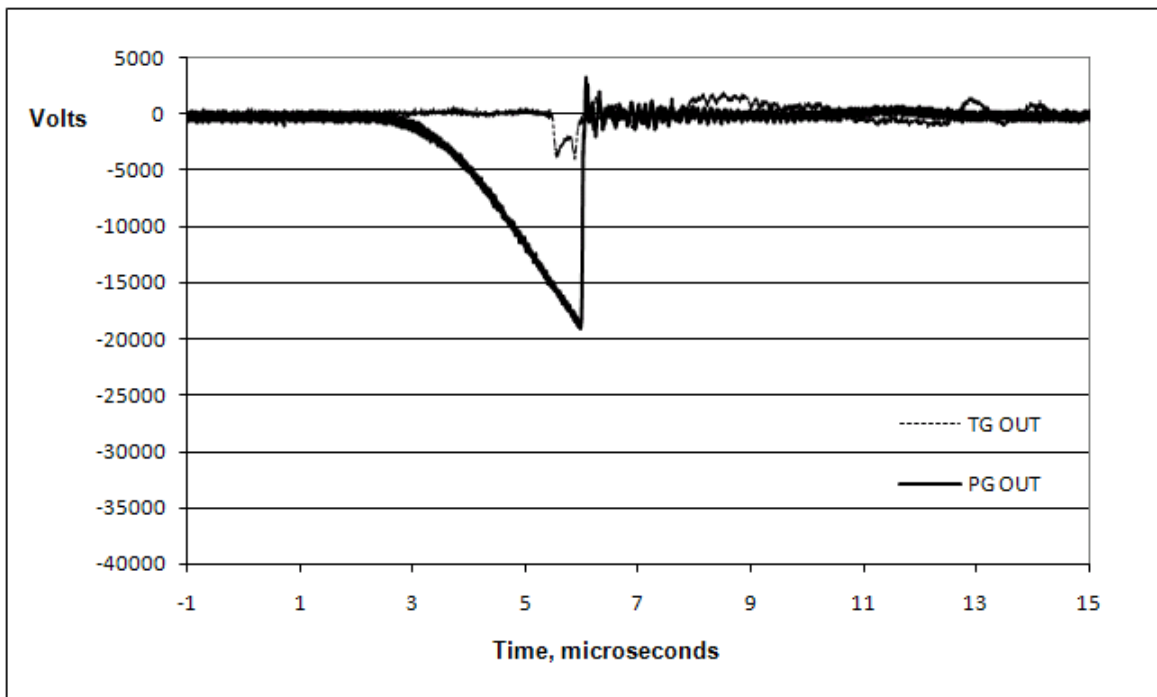


**Figure C-5.** Voltages from Delay Trigger Generator and High-Voltage Pulser Using Pulsed E-Beam Gun with Two Capacitors. Conditions: 3.1-nF Total Capacitance, 71-mtorr Gun Pressure, 57.5-mtorr Cell Pressure, 60% Dial Settings for Both Units.

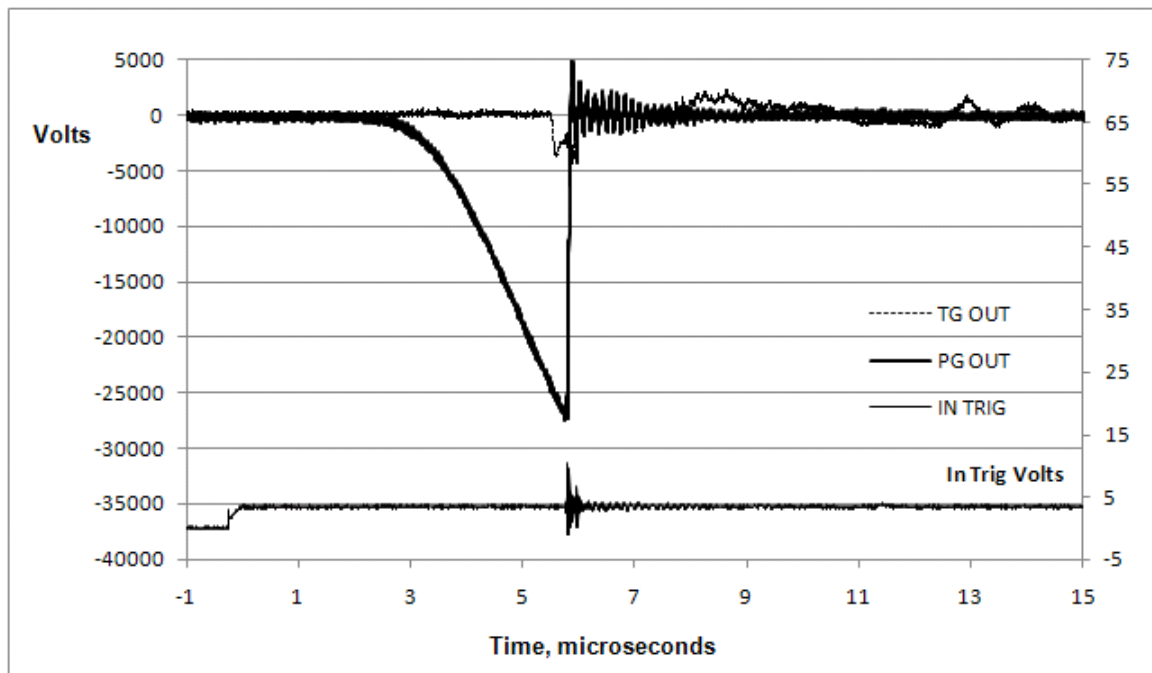


**Figure C-6.** Voltages from Delay Trigger Generator and High-Voltage Pulser Using Pulsed E-Beam Gun with One Capacitor. Conditions: 1.5-nF Capacitance, 70-mtorr Gun Pressure, 46-mtorr Cell Pressure, 60% Dial Setting for Both Units.

## APPENDIX C. CONTINUED



**Figure C-7. Photograph of Discharge from Pulsed E-Beam Gun, with Two Capacitors, into Static Cell with 40-mtorr Air. Gun Pressure at 60-mtorr, 70% Setting for High-Voltage Pulser (25 kV Max Voltage).**

## IMPROVEMENT 2: RESPONSE TIME REDUCTION

It is desirable to reduce the response time of the pulsed e-beam system, where the response time is the time between the receipt of a trigger signal sent to the system and the time that the pulsed e-beam fires from the transiently opened aperture of the FARVA. Since there is only an approximately 6- $\mu$ sec delay time for the high-voltage pulse d e-beam electronics, the FARVA operational time will determine the overall system response time. Referring to Fig. 16, there is a nominal delay time of 1.2 milliseconds for the FARVA valve assembly. In order to reduce this time, two improvements to the FARVA unit were performed: 1) install a heavier duty motor controller to drive the high-torque motor that actuates the valve and 2) install a stiffer connecting shaft between the motor and the valve disk. Figure 13 shows the mechanical arrangement of the FARVA, and the high-torque motor can be seen at the top of the FARVA and the existing plastic shaft which connects the motor to the thin, aluminum disk that acts as the pressure barrier between the low-pressure gun and the high-pressure test medium.

To produce the heavy-duty motor drive circuit, five “ganged” National Semiconductor LMD18200 motor drivers are arranged in parallel. This arrangement was developed to replace the previous system’s off-the-shelf module that exhibits excessive delay from the drive command signal to valve opening. Activation of the new heavy-duty circuit was controlled by an Agilent 33220A function generator to eliminate delay inherent in the Copley control system. The laboratory arrangement is shown in Fig. 35.

## APPENDIX C. CONTINUED

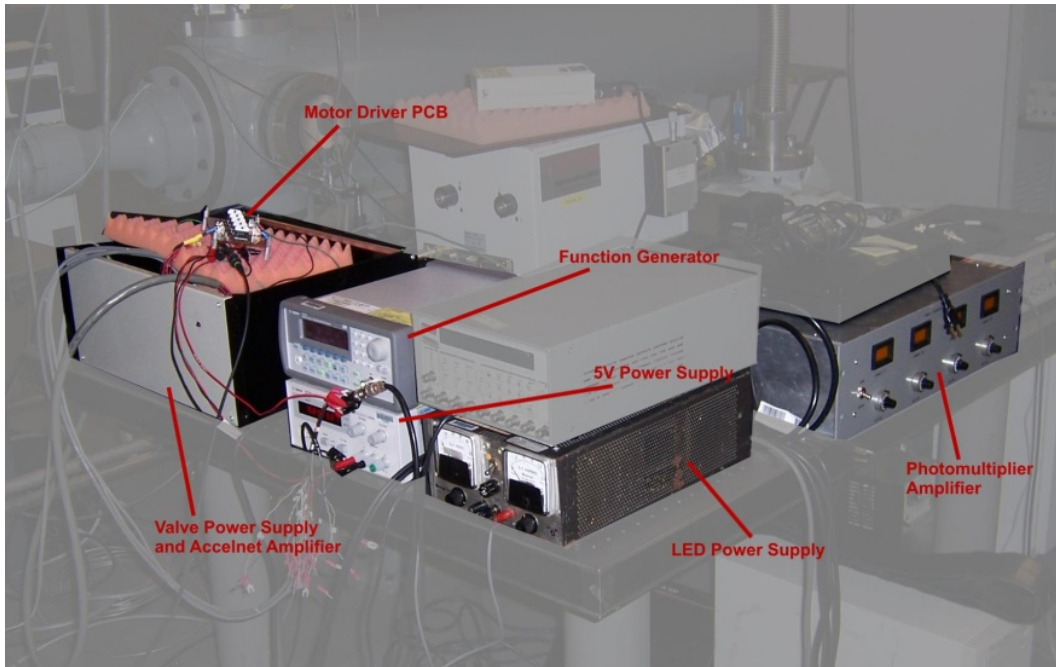


**Figure C-8. Equipment Arrangement for Modified Motor Drive Circuit.**

An additional system modification was replacement of the drive shaft connecting the valve motor to the valve disk. The original shaft was made of Lexan or similar plastic material, possibly turned from stock to the finished diameter. The new shaft was made of 0.375-in.-diam carbon fiber rod cut to length.

Results indicate the new circuit was successful. The best-case delay of the original Copley Accelnet servoamp module with valve “windup” or preset position at 4.3° (72 encoder counts) in front of the valve open position was 8.20 milliseconds. Under the same windup, a delay of 3.66 milliseconds was measured using the new circuit and carbon fiber shaft. This is relevant since the shock tube sequence of events lasts only about 8 milliseconds.

A detailed comparison at other conditions is listed in Table C-2. Again referencing Fig. 13, it can be seen that in addition to the e-beam aperture of the valve disk, there is a second aperture that is 180 deg away. This second aperture is used as a trigger by allowing light from a continuously emitting LED to be coupled into an optical fiber. This fiber optic signal is labeled in the table as FO2. Another fiber optic signal system (not shown in Fig. 13) that is located 10 deg “upstream” of the FO2 system provides another trigger (FO1) that occurs before the FO2 signal. Shaft twist was calculated from the difference of the motor encoder and the valve position as detected by the fiber optic signals while the valve is running.

## APPENDIX C. CONTINUED

**Table C-2. FARVA Time Response Data for Various Initial Positions and Equipment Configurations.**

Windup Counts	Supply Volts	Shaft Driver	FO1 delay, msec	FO1 twist, counts	FO2 delay, msec	FO2 twist, counts	FO2 twist, degree	Motor velocity at FO2, rpm
72	31.5	plastic Copley			8.20	812	48.72	1350
100	31.5	plastic Copley			9.59	884	53.04	1850
272 31.5		plastic Copley			10.60	924	55.44	825
472 31.5		plastic Copley			11.96	686	41.16	708
72 31.5		carbon fiber LMD 18200			3.66	246	14.76	780
100 31.5		carbon fiber LMD 18200			3.32	211	12.66	923
166 31.5		carbon fiber LMD 18200			4.40	189	11.34	539
271 31.5		carbon fiber LMD 18200	3.31 32		4.51 245		14.7	1358
439 31.5		carbon fiber LMD 18200	3.4 30		4.90	-24	-1.44	841
472 31.5		carbon fiber LMD 18200	5.78 300		5.78 587		35.2	1957
642 31.5		carbon fiber LMD 18200	5.5 4		6.60	-8	-0.48	1681
166 44		carbon fiber LMD 18200			3.95	368	22.08	1081
273 44		carbon fiber LMD 18200	2.8 243		3.98	216	12.96	1395

The table shows that for the original system that used the plastic shaft and Copley motor controller the disk velocity (when its aperture passed by the e-beam outlet) has a velocity of 1,350 rpm at the smallest windup (72 counts). The lowest speed recorded for the plastic shaft is 708 rpm at a 472-count windup. It was expected that the fastest velocity would have been for the largest windup value, assuming that the motor can achieve a faster speed when given more time to accelerate. However, this assumption was not borne out in the experimental results. This phenomenon is noticeable in Fig. C-9, which shows that the calculated motor velocity exhibits several relative maxima and minima in the 50-millisecond time period shown on the graph. The nonlinear velocity-time response can be attributed to the elasticity of the plastic shaft. Figure C-9 is for a 100-count (6-deg) windup situation.

The shaft twist at the moment the disk aperture passes the e-beam outlet can be measured by comparing the known angular position of the disk (0 deg) with the angle provided by the encoder at the other end of the shaft. The twist angles for the plastic shaft are fairly severe and are around 50 deg for the four test conditions listed in the table. In Fig. C-9 the time for the actual opening of the e-beam output is approximately 9.6 millisecond s after the trigger to the FARVA curs (Input 6); however, the motor encoder shows that it begins moving 5

## APPENDIX C. CONTINUED

milliseconds after receipt of the start trigger. The remaining 4.6 milliseconds are associated with the time required to twist the plastic connection rod and to move the aperture to the correct angular position.

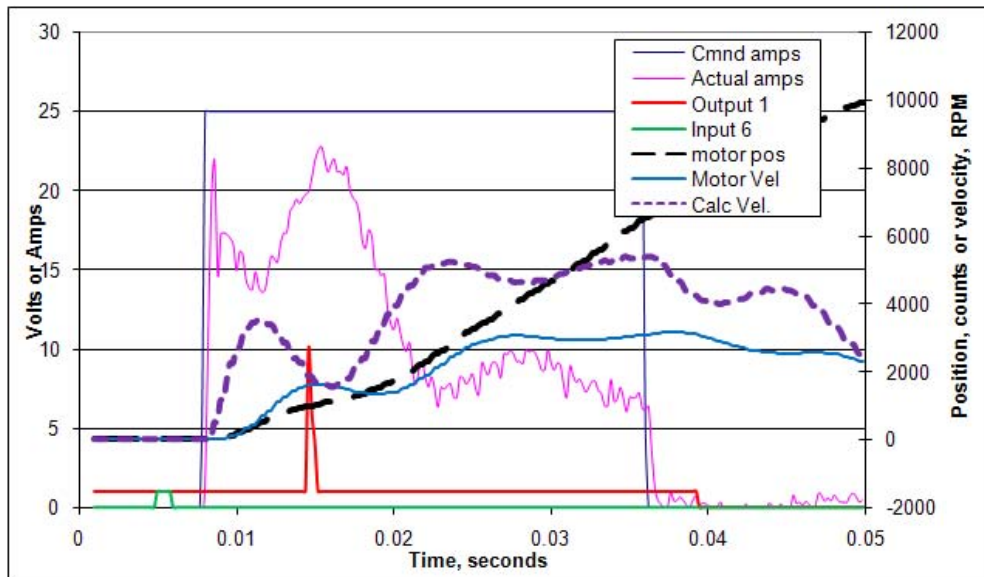


**Figure C-9. FARVA Valve Response Data with Copley Accelnet Drive Circuit and Plastic Drive Shaft. Data is for a 100-Count (6-deg) Windup Situation. Green Pulse is Start Command. Red Spike is Estimated Valve Opening Time Merged from Other Data Source. Motor Velocity Data are Provided Directly by Copley Control Software. Calculated Velocity Data are Obtained from Motor Position Data and Times Associated with that Data.**

By replacing the plastic shaft with a stiffer carbon-fiber shaft, the delay time associated with the twisting of the shaft was greatly reduced. The twist angles using the carbon-fiber shaft are also greatly reduced, as shown in Table 2. They have dropped to a nominal value of approximately 16 deg or less, as compared to the 40- to 55-deg range of the plastic shaft. In addition, the new power supply that provides power to the motor has been improved by using the LMD18200-based power supply. These two modifications, along with the use of an Agilent 33220 A controller rather than the relatively slow Copley controller, have greatly reduced the delay time for the FARVA. For example, with a 272-count (16-deg) windup and 31.5-volts supply voltage, the original system had a time delay of 10.6 milliseconds, whereas the new system had only a 4.51 millisecond time delay. By increasing the supply voltage from 31.5 to 44 volts, the time delay is decreased to an even smaller value: 3.98 milliseconds. Figures C-10 and C-11 show data obtained from the FARVA when it operates with the stiffer shaft and new motor driver. For these figures the time delay between the arrival of the trigger signal (Input 6) and the opening of the aperture to the e-beam (Output 1) is approximately 4 milliseconds.

### OBSERVATIONS:

In the previous section it was shown that the replacement of the original plastic shaft with a carbon-fiber shaft and the replacement of the Copley motor controller with a custom-made, heavy-duty motor controller greatly reduced the time delay of the FARVA. During the testing of the FARVA, the following additional observations were made:

## APPENDIX C. CONTINUED

1. Vacuum conditions with pumps running vs. no pumping showed no significant speed difference. Therefore, all test data were obtained with no pumping since this was easier to execute.
2. Velocity data reported by the Copley servo amplifier user interface appear to be inaccurate, possibly due to excessive filtering. The velocity data appear delayed and smoothed relative to velocity calculated using encoder position and time which correlated inversely with motor current.
3. Although the carbon fiber shaft flexes torsionally (twists) as evinced by difference in position indicated by motor encoder from the position indicated by valve aperture wheel, it does so much less than the plastic shaft.
4. An increase in supply voltage of 13 volts using a lead-acid battery did not show appreciable speed benefits at short windups. This may have been due to significant battery voltage drop when the valve was moved.
5. Calculated velocity plots indicate it takes 1 millisecond for the motor to spin up freely (take up slop) then another millisecond before velocity minimizes, probably when the shaft has torqued and valve static friction is overcome resulting in valve movement. Therefore, it is unlikely that any reduction of opening time under 2 milliseconds can be made no matter how small the windup.

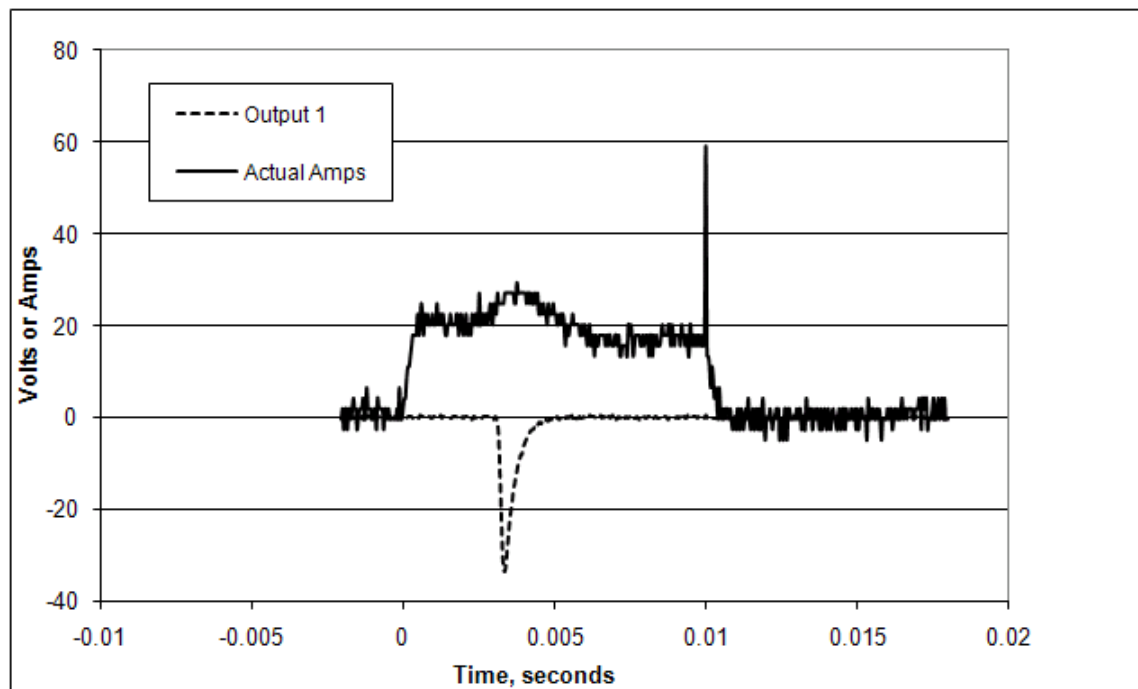


**Figure C-10. FARVA Valve Response Data when Using LMD18200 Drive Circuit and Carbon Shaft. Data are for a 100-Count (6-deg) Windup. Output 1 is LED Signal (FOS2) Indicating Aperture Opening for E-Beam. Measured Amperage is That Entering FARVA Motor.**

## APPENDIX C. CONTINUED

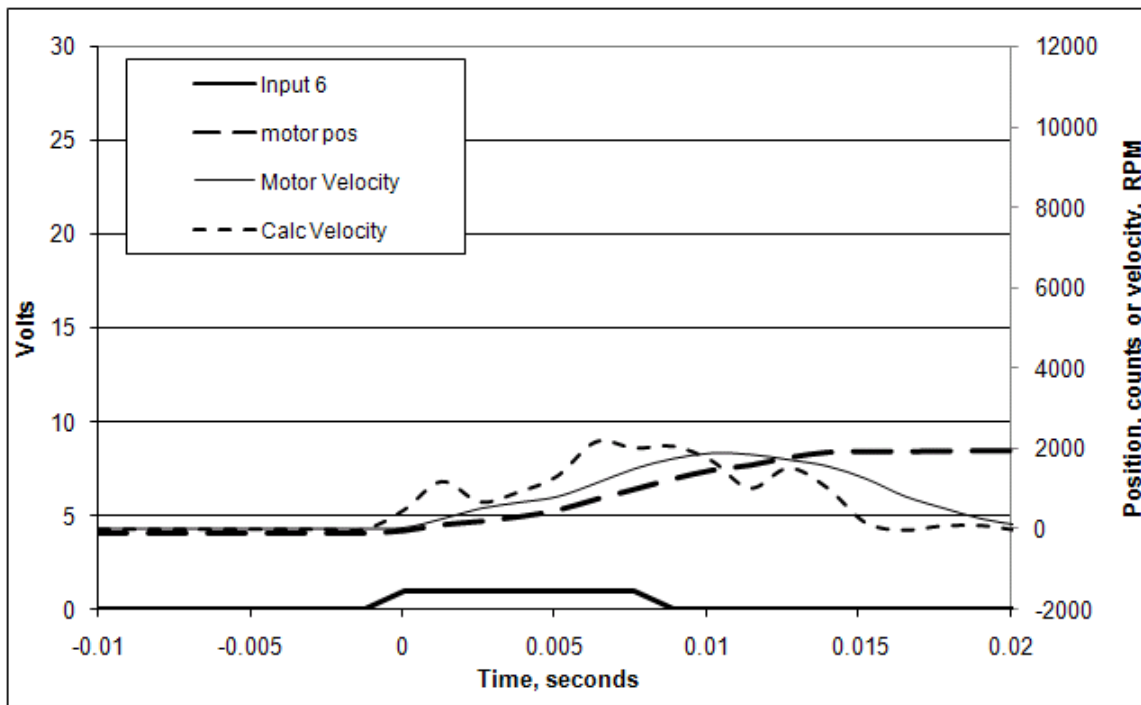


**Figure C-11. FARVA Valve Response Data when Using LMD18200 Drive Circuit and Carbon Shaft. Data is for a 100-Count (6-deg) Windup. Input 6 is Start Command, Which Occurs at 0 sec. Motor Position and Motor Velocity Data Obtained from Encoder on Motor Along with Encoder Software. Calculated Velocity Obtained from Motor Position Data and Known Times.**

### IMPROVEMENT 3: OPTIMUM APERTURE SIZE

The original pulsed e-beam system includes a fast action valve assembly (FARVA) whose major pressure barrier is a thin aluminum disk with a 0.125-in.-diam aperture that acts as the transiently opened aperture through which the pulsed e-beam travels. Figure C-1 2 shows a photograph of the FARVA disk. The aperture is shown at the bottom of the wheel, and another smaller hole, used for triggering purposes, is at the top of the disk. Large cutouts on the wheel reduce the disk's moment of inertia. The 0.125-in. aperture provides a 150- $\mu$ sec opening time when the 4.5-in.-diam disk is properly positioned to open at the fastest speed provided by the high-torque FARVA motor.

## APPENDIX C. CONTINUED



**Figure C-12. Photograph of Original Rotating Disk in FARVA Showing 0.125-in.-diam Aperture at Bottom and Smaller Aperture Used for Timing Purposes at Top.**

Several considerations affect the optimum orifice diameter. One consideration is that as the hole is made smaller, it takes a longer time for the pulsed e-beam gun to fill with gas for a given ambient pressure. Thus the gun has a better chance to successfully fire. However, as the aperture is made smaller, a lower percentage of the pulsed e-beam discharge makes it out into the ambient environment. At the other extreme, for a large-diameter orifice, there will be no reduction in the amount of electrons passing through the hole, but the gun will be quickly pressurized to the same pressure as the test medium into which it fires as soon as the valve opens. Obviously the two extremes of a very large- or a very small-diameter aperture do not provide a useful output for the pulsed e-beam system. For an infinitely small aperture, the gun will remain at its optimum pressure (approximately 70 mtorr), but no electrons will be emitted. For an infinitely large aperture, the gun will not even fire for an ambient pressure significantly above 70 mtorr. Thus, for a given hole size and rotational speed, there is an optimum aperture size that will give the strongest issuance of electrons out of the FARVA.

In addition to the original disk, two additional disks were machined. Each of the new disks had the same overall diameter as the original, but one new disk had an orifice that was 50% larger than the original, and the other new disk was 50% smaller. The two new disks were also slightly thicker and did not have the metal cutouts that the original disk had, so their moments of inertia were significantly larger than that of the original disk. The expectation for these disks is that the largest diameter (0.1875-in.) aperture will provide the strongest e-beam output at low pressures, but at the cost of lowering the maximum pressure for the test medium that the e-beam shoots into. Conversely, the smallest diameter (0.0625-in.) aperture will provide the weakest e-beam output of the three apertures, but will be able to provide an e-beam for test medium pressures that are above those associated with the other two larger orifices. As mentioned earlier in this report, the upper pressure limit for the original 0.125-in.-diam aperture is 50 torr. Thus the largest aperture is expected to allow pulsed e-beam operation up to a maximum pressure that is below 50 torr, and the smallest aperture will allow operation up to a maximum pressure above 50 torr.

The largest diameter (0.1875-in.) aperture disk was tested first. The pulsed e-beam system was mounted on the Laboratory Shock Tunnel dump tank, which acted as a static cell that could be pressurized with air or nitrogen. For this test, air was used as the test medium. As expected, the maximum static cell pressure that would still allow successful e-beam emission was significantly lowered. The pulsed e-beam operated reliably up to approximately 2 torr, but

## APPENDIX C. CONCLUDED

output strength and shot-to-shot repeatability degraded as the static cell pressure was increased to 5 torr. Above 5 torr no e-beam emission could be visually observed, and no N<sub>2</sub><sup>+</sup> emission spectra could be recorded using the spectrometer and CCD camera. However, within its operation range the 0.1875-in.-diam aperture allowed more electrons to be emitted by the pulsed e-beam gun than the original 0.125-in.-diam aperture. For example, Fig. C-13 shows an emission spectrum obtained by firing the pulse d e-beam gun with the large-diameter aperture into 0.5-torr air. The signal strength is excellent for this situation. The signal-to-noise ratio for this spectrum is much better than for the spectra taken at 0.65 torr which are shown in Figs. 23a and 23b. In Fig. 40 the N<sub>2</sub><sup>+</sup> and N<sub>2</sub> emission bands are all clearly visible with much less random variations in the signal strength across the spectrum in comparison to those in Fig. 23.

Next, the disk with the 0.1875-in. orifice was replaced by the one with the 0.0625-in.-diam orifice. Unfortunately, as this disk was being checked out for testing, the power supply for the high-torque valve motor experienced a catastrophic failure which put an early end to this, the last task of the follow-on work. The replacement of the damaged power supply was prohibitively expensive and would require too long of a delivery time to be accomplished within the scheduling and cost limits of the follow-on project. As a result, the 0.0625-in.-diam orifice disk has not been experimentally investigated.

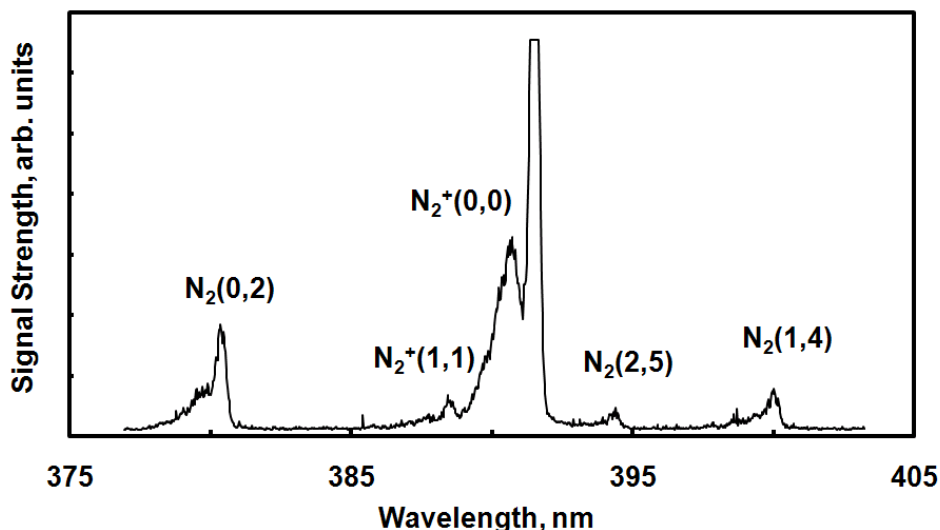


**Figure. C-13. Nitrogen Emission Spectrum from 0.5-torr Air in Laboratory Shock Tunnel Dump Tank Using Pulsed E-Beam System with Large-Diam (0.1875-in.) Aperture in Fast Action Valve Assembly (FARVA).**

To summarize this add-on task, the 0.1875-in.-diam aperture allows the pulsed e-beam system to operate only up to 5 torr for the test medium pressure. In comparison, the 0.125-in.-diam aperture allows the system to operate up to 50 torr, a full order-of-magnitude higher. However, for pressures below 2 torr the 0.1875-in.-diam aperture provides a stronger e-beam than does the 0.125-in.-diam aperture.